

**UNIVERSITY OF BRISTOL**

**DEPARTMENT OF  
ENGINEERING MATHEMATICS**



**INFLUENCE OF STABLE MANIFOLDS  
ON  
PHASE-RESETTING IN EXCITABLE CELLS**

**Siti Hasmah Mazlan (Engineering Mathematics)**

Project thesis submitted in support of the degree of  
Master of Engineering

**Supervisors:**

**Dr Hinke Osinga, Dr Krasimira Tsaneva-Atanasova**

**Engineering Mathematics *June 2008***

## ABSTRACT

This project deals with the study of bursting in somatotrophs cells. As it is widely accepted, the bursting mechanism can be explained by considering the so-called fast subsystem, where one of the variables that actually varies very slowly compared to the other variables, is assumed to remain constant. The associated bifurcation diagram of the fast subsystem then explains the transitions from the silent phase to the active bursting phase. In our model, the correspondence of the bifurcation diagram and the bursting behaviour is not so clear and certain features are not explained at all. We show here that the inclusion of basin boundaries of the fast subsystem does provide a satisfactory explanation, particularly of the termination of the bursting phase.

We also investigate how an external perturbation affects the behaviour of the cell. We show that the dynamics again is determined by the basin boundaries along with the bifurcation diagram of the fast subsystem. However, the fast subsystem does not fully explain the effect of perturbation. In particular, one cannot draw conclusions on the time it takes for the system to settle back to the unperturbed state and, therefore, we cannot deduce the change in the phase of the bursting pattern. However, by using a normal form analysis near a saddle-node bifurcation in the fast subsystem, we are able to give some insight into how the strength of the perturbation influences the time it takes to cause a potentially large change in the phase.

## **TABLE OF CONTENTS**

<b>SECTION 1</b>	<b>INTRODUCTION</b>	4
<b>SECTION 2</b>	<b>DYNAMICAL SYSTEM ANALYSIS</b>	6
2.1	Cell model and the dynamics interpretation	6
2.2	Analysis of the fast subsystem	9
2.2.1	Oscillations below spiral nodes	14
2.2.2	Ending the active phase before homoclinic bifurcation	16
2.3	Stable manifolds computation	16
<b>SECTION 3</b>	<b>PHASE-RESETTING</b>	20
3.1	Definition and procedures	20
3.2	Resetting in the fast subsystem	21
3.1.1	Properties of the applied current	21
3.1.2	Change in the bifurcation structure	22
3.1.3	Duration to cross basin boundary	26
3.3	Dynamic resetting in the full system	29
<b>SECTION 4</b>	<b>ROLE OF THE STABLE MANIFOLDS</b>	33
<b>SECTION 5</b>	<b>DISCUSSION AND CONCLUSION</b>	36
	<b>REFERENCES</b>	38
	<b>APPENDIX</b>	40

## SECTION 1 INTRODUCTION

Excitable cells are biological entities that can be stimulated to induce electrical periodic bursting activity. This bursting activity is vital for cellular physiological functions such as processing information and interactions, within and between cells [8]. Failure in the regulation of cells can cause undesirable effects for the cells to function normally. For instance, dysfunction of the excitable cells in the brain is recognised to cause Alzheimer's disease [10]. Therefore, this demands understanding of the excitable behaviour of such cells.

There have been many works by physiologist and mathematicians to understand the excitable behaviour of the cells. Among these, in 1952, Hodgkin and Huxley [6] had successfully derived a mathematical model to describe this excitable behaviour using the nervous system excitable cell, the neuron. Nevertheless, the actual physiological properties remain an area of active research due to the degree of complexity of this classical model. It was not until 1985 that Rinzel [11] had proposed the qualitative methods to interpret the behaviour of the excitable cells.

Apart from bursting behaviour, it is also useful to understand the mechanism of resetting the phase or rhythm of excitable cells (or periodic behaviour). Using the excitable cardiac cells, Winfree significantly contributed to the qualitative understanding on the phase-resetting technique by showing that a particular amount of external stimulus can cause irregular heartbeat rhythm. Such predictions can be made even without the biological details [15]. In this case, the application of phase-resetting may be beneficial in terms of predicting failure of cells. In other instances, resetting the phase has shown profound effects in repairing the damage caused by the abnormal rhythm of cells; see [2] for more details. Thus, resetting the rhythm of the cells' periodic behaviour potentially results in positive or negative effects, depending on the amount of stimulus and the type of cell. On this basis, Stern et al [12] had refined this approach to reflect qualitative changes by using bifurcation analysis in their analysis of excitable cells.

This project primarily focuses on the bifurcation analysis and phase-resetting methods as explored by [12]. The bifurcation analysis describes qualitative changes and instabilities in the system solution as a control parameter is varied. The term phase-resetting, on the other hand, is a change in the rhythm of the periodic solution caused by the application of an

external stimulus. Stern and co-workers attempted to analyse how the amount of external electrical current alters the rhythm of the model's solution, with the aim to distinguish different classes of cell models. However, the feasibility of the methods by [12] in terms of the actual physiological application is uncertain because their model lacks the effects of an ionic channel in the cells; namely the BK-channels. The model presented by Tsaneva-Atanasova et al. [14] incorporates the function of BK-channels and demonstrates a better match with experimental data. Nonetheless, this model also greatly shortens the burst period, which calls question on the scientific value of the results in [12]. In this project, we consider a simplified version of the model derived in [14] and investigate the consequences on the aforementioned methods

This thesis is organised as follows. In **Section 2**, we present an adaptation of the cell's model from [14] and describe the techniques of bifurcation analysis. We compute stable manifolds and show how they organise the dynamics. We then proceed with the phase-resetting technique in **Section 3**, where we provide an explanation on the method of phase-resetting and estimate the appropriate amount of external electrical current. Finally in **Section 4**, we consider the effect of the BK-channels to demonstrate any physiological relevance.

We evaluate the mathematical equations of the model in the Maple environment and simulate the numerical solutions in XPP [4] and Matlab [5] interfaces. All visualisations are carried out in the Matlab environment. The bifurcation diagrams are computed using the continuation package AUTO [3].

## SECTION 2: DYNAMICAL SYSTEM ANALYSIS

### 2.1 Cell model and the dynamics interpretation

We use qualitative approaches to study a model that describes the mechanism of excitability in a cell. The motivation of this study comes from techniques of bifurcation analysis and phase-resetting employed by Stern et al. [12]. To match these techniques, we refer to the model derived by Tsaneva-Atanasova et al. [14]. They provide a mathematical model for the bursting mechanism in somatotroph cells. These brain cells release growth hormone in the pituitary gland [1]. **Figure 2.1** shows the location of the gland in the human brain.

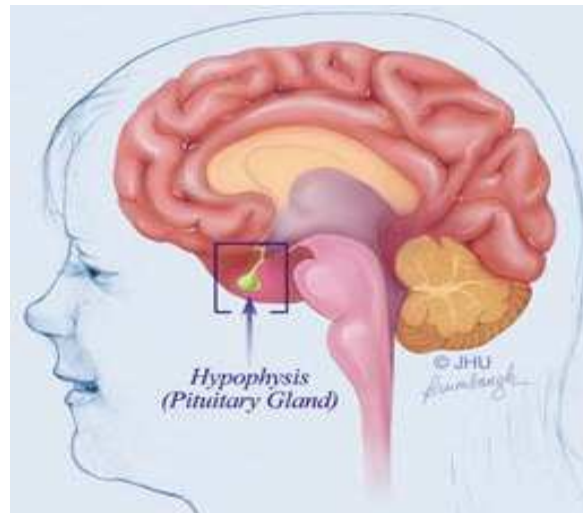


**Figure 2.1** Pituitary gland reproduced from Johns Hopkins University School of Medicine & Johns Hopkins Health System. ([www.pathology2.jhu.edu](http://www.pathology2.jhu.edu))

The model in [14] is slightly different from the model in [12], because one of the calcium-dependent channels in the cell (BK-channels) can be partially blocked. At first glance, this only results in a minor change in the bifurcation structure, but the obstruction exerts a significant influence in shortening the cell's bursting period. The phenomenon was not observed in the model studied by [12]. We believe the invariant stable manifolds are the actual mechanism that determines termination of the bursting process. By employing a more realistic model from Tsaneva-Atanasova et al. [14], we verify this conjecture and deduce whether techniques of bifurcation analysis and phase-resetting employed by [12] are still relevant for this more realistic model of an actual biological cell. The model from [14] also allows us to investigate the influence of the ion regulation across the BK-channels on the bursting behaviour.

The modified model is described as a set of coupled non-linear ordinary differential equations (ODE) with three time-dependent variables: the membrane potential  $V$ , concentration  $Ca$  of intracellular  $Ca^{2+}$  ions, and the fraction  $n_{dr}$  of open potassium channels. The ODE can be expressed as

$$\left. \begin{aligned} \dot{V} &= \frac{dV}{dt}(V, n_{dr}, Ca) = \frac{1}{c_m} (-I_{ionic} + I_{app}) ; \\ \dot{n}_{dr} &= \frac{dn_{dr}}{dt}(V, n_{dr}) = \frac{n_{dr_{\infty}}(V) - n_{dr}}{\tau_{n_{dr}}} ; \\ \dot{Ca} &= \frac{dCa}{dt}(V, Ca) = \gamma I_{Ca}(V) + J(Ca) ; \end{aligned} \right\} \quad (1)$$

where

$$I_{ionic} = I_{Ca}(V) + I_{Na}(V) + I_K(V, n_{dr}) + I_{bk}(V, Ca). \quad (2)$$

The first ODE in equation (1) is formed by an expression of the ionic currents  $I_{ionic}$ , which can be altered via an applied current  $I_{app}$ ; we set  $I_{app} = 0$  in the first part of our project. These two currents are divided by a membrane capacitance  $c_m$  to give the rate of change  $\dot{V}$  with respect to time. As indicated in equation (2), the current  $I_{ionic}$  comprises of non-linear functions  $I_{Ca}$ ,  $I_{Na}$  and  $I_K$  that describe the currents flowing through the calcium, sodium and potassium channels, respectively. Furthermore,  $I_{ionic}$  includes an expression of current flow through the BK-channels, denoted as  $I_{bk}$ . For a start, we assume that the BK-channels are blocked by 0%. The rate of change of the second variable  $n_{dr}$  is governed by a voltage-dependent steady-state function  $n_{dr_{\infty}}$  and  $n_{dr}$  itself. The difference between  $n_{dr_{\infty}}$  and  $n_{dr}$  is divided by the time  $\tau_{n_{dr}}$  that it takes for  $n_{dr}$  to reach its steady state, to give the equation for  $\dot{n}_{dr}$ . Finally,  $\dot{Ca}$  is determined by a direct relationship with the change in  $Ca$  and  $V$ . Precise definitions of the right-hand sides are given in the **Appendix**.

The ODE in equation (1) can be solved numerically using a number of integrators in XPP and Matlab. We found that Matlab has problems solving the ODE using ode45, because the ODE is rather stiff [2]. Therefore, we choose the ‘stiff’ solver in XPP and ode15s in Matlab. The order of error tolerance for ode15s is also reduced to  $10^{-12}$ .

Integrating the ODE in equation (1) with any arbitrary initial condition always results in a solution that settles on the same closed curve in the phase space. From a dynamical system's point of view, this similar eventual periodic behaviour means that there exists a globally attracting periodic orbit in the system. Hence, every initial condition eventually settles on this closed curve, though the time series may be out of phase. **Figure 2.2(a)** shows time series in both  $Ca$  and  $V$  of the eventual periodic motion, while the global periodic attractor as a closed orbit is shown in **Figure 2.2(b)**.

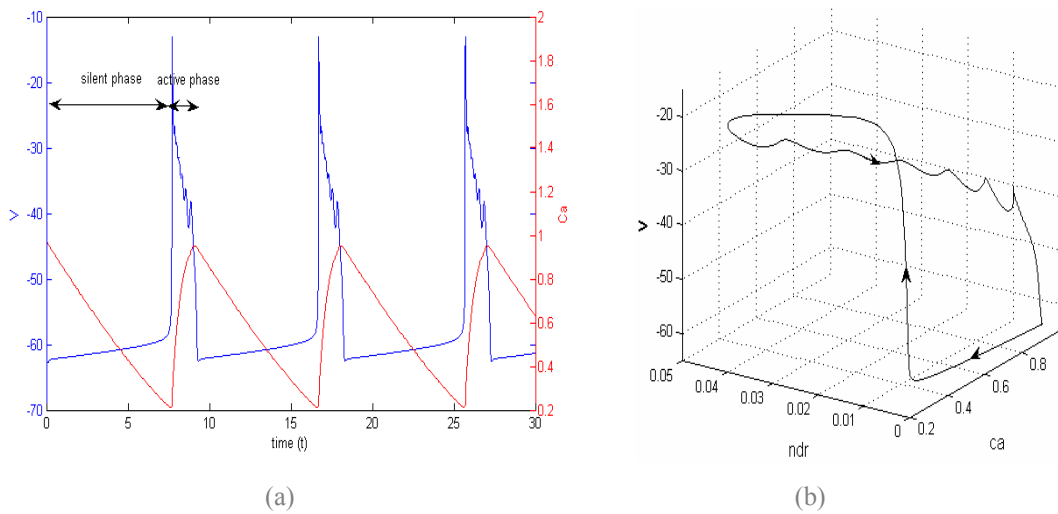


**Figure 2.2** Panel (a) shows the time series for  $Ca$  and  $V$  over a time interval of 30s. The globally attracting periodic orbit is shown in panel (b), with arrows indicating the orbit direction with respect to time.

The solution exhibits periodic behaviour, as shown by the time series in **Figure 2.2(a)**. Within each period,  $Ca$  alternately rises and declines steadily between approximately  $0.2 \mu M$  and  $1.0 \mu M$ . The membrane potential  $V$  rises only slightly during the fall of  $Ca$  but rapidly shoots up and fires a train of small spikes that damp down towards decreasing  $V$ , before plunging to approximately  $-65 mV$  and repeating the process.

We relate our solution with the cell's behaviour where a cell is said to be at rest or in the silent phase when there is no bursting activity. The silent phase corresponds to the straight segment of the periodic orbit in **Figure 2.2(b)**, where  $V$  is approximately  $-65 mV$  and  $n_{dr}$  is about  $0.005$ . As the orbit follows the arrows, the system enters an active phase with a relatively high  $V$  and starts to have a rise in the  $Ca$  concentration. Within two seconds, a burst with some small spikes is fired until the  $Ca$  concentration reaches its peak value.

The active phase terminates after  $Ca$  begins to decrease again. Termination of the active phase completes the cycle.

The time series in **Figure 2.2(a)** indicates the presence of two different time scales. While  $Ca$  always varies rather slowly,  $V$  fluctuates very fast during the active phase. We can also deduce that  $n_{dr}$  is a fast variable, as the periodic orbit in **Figure 2.2(b)** fluctuates in the  $n_{dr}$  direction as well during the active phase. Rinzel [11] has introduced a method to study this type of fast-slow system. The basic idea is to reconstruct the system by describing the fast dynamics of  $n_{dr}$  and  $V$  with the slow variable  $Ca$  treated as a parameter, i.e., by setting  $\dot{Ca} = 0$ . We then identify the stability properties of the fast subsystem for the range of values visited by  $Ca$ . Finally, the full system is re-analysed to conclude the influence of the slow  $Ca$ -dynamics on the alternating behaviour of the system between a silent and an active phase.

## 2.2 Analysis of the fast subsystem

As we eliminate the expression of  $\dot{Ca}$  in equation (1), we now have a fast subsystem with two ODEs

$$\left. \begin{aligned} \dot{V} &= \frac{dV}{dt}(V, n_{dr}) = \frac{1}{c_m} (-I_{ionic}(Ca, n_{dr}, V) + I_{app}) \quad ; \\ \dot{n}_{dr} &= \frac{dn_{dr}}{dt}(V, n_{dr}) = \frac{n_{dr_{\infty}}(V) - n_{dr}}{\tau_{n_{dr}}} \quad . \end{aligned} \right\} \quad (3)$$

Each equilibrium point that exists at a particular value of  $Ca$  is found as the intersection points of the  $n_{dr}$ - and  $V$ -nullclines. These nullclines are curves that satisfy either  $\dot{n}_{dr} = 0$  or  $\dot{V} = 0$  [13]. From equation (3), we obtain the  $V$ -nullcline as a continuous function that spans across all  $n_{dr}$ -values. Similarly the  $n_{dr}$ -nullcline continuously spans across all  $V$ -values. Therefore, the subsystem will have at least one equilibrium point because both nullclines will always intersect for different values of  $Ca$ .

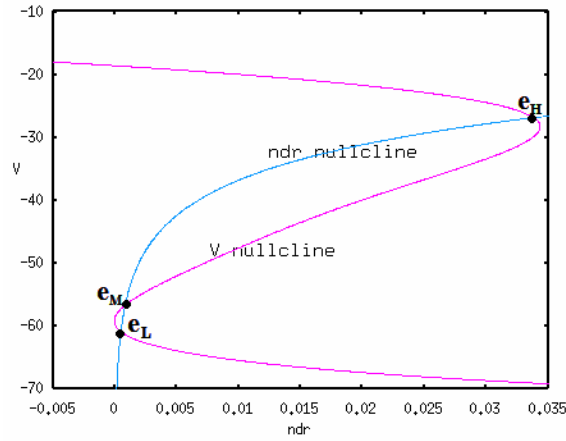


**Figure 2.3** The  $n_{dr}$ - and  $V$ -nullclines for  $Ca=0.5\mu M$ . The equilibria at the intersection points of the nullclines are denoted  $e_L$  (low),  $e_M$  (middle) and  $e_H$  (high).

**Figure 2.3** shows the nullclines for  $Ca = 0.5\mu M$ . As illustrated in the figure, the subsystem has three equilibria, represented by the intersection points  $e_L$ ,  $e_M$  and  $e_H$ . Since the equation  $\dot{n}_{dr} = 0$  does not contain the parameter  $Ca$ , the  $n_{dr}$ -nullcline (violet) will always retain the same shape, regardless of the value of  $Ca$ . The Z-shape of the  $V$ -nullcline (green), however, transforms when  $Ca$  changes. If the parameter increases, the upper knee is pushed towards the left-bottom corner of the plane, while the lower knee hardly moves at all. The equilibria  $e_M$  and  $e_H$  then move closer and finally coalesce in a saddle-node bifurcation. After the bifurcation, they disappear and the lower equilibrium  $e_L$  remains as the only equilibrium in the fast subsystem. **Figure 2.4** shows the nullclines after  $Ca$  increases to  $2.0\mu M$ , with  $e_L$  as the only equilibrium point.

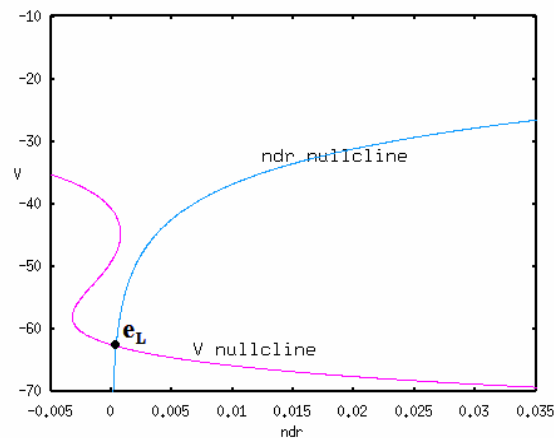


**Figure 2.4** The  $n_{dr}$ - and  $V$ -nullclines for  $Ca=2.0\mu M$ ; compare also with **Figure 2.3**.

When  $Ca$  decreases from  $0.5\mu M$ , the  $V$ -nullcline does not lose its cubic structure. The upper knee of the nullcline moves to the right while the lower knee shifts only slightly in

the same direction. Another saddle-node bifurcation happens when the lower knee intersects the  $n_{dr}$ -nullcline tangentially. After this bifurcation, the fast subsystem will have  $e_H$  as the only equilibrium point.

We obtain all equilibria along with their stability properties by continuation in  $Ca$  using the package AUTO. **Figure 2.5** summarises the numerical bifurcation diagram.

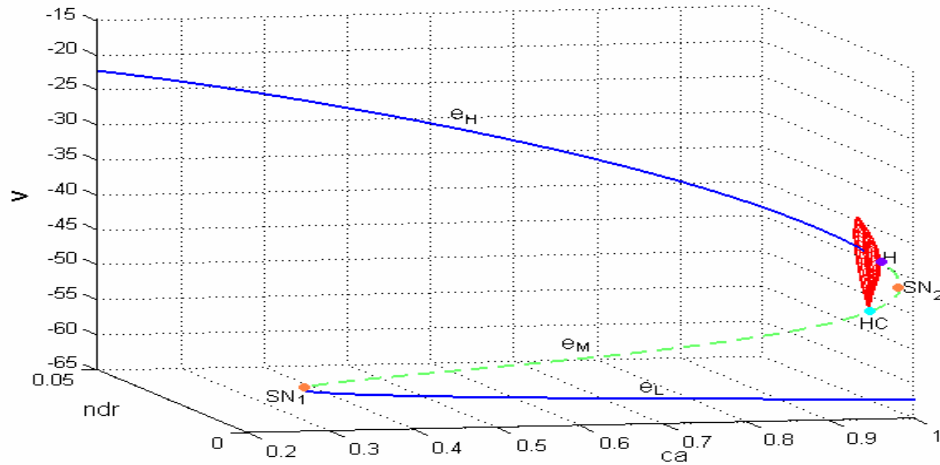


**Figure 2.5** Matlab visualisation of the bifurcation diagram, created with AUTO. The blue and green dotted lines are the respective stable and saddle equilibria of the fast subsystem. There exists a family of unstable limit cycles, portrayed by the red hemisphere on the right of the picture. The bifurcations points are labeled with thick dots.

We start AUTO from a point on the branch  $e_H$  for  $Ca = 0.2\mu M$  and trace a Z-shaped curve that stops at our defined boundary  $Ca = 1.0\mu M$ . Along the curve, AUTO detects one Hopf (H) and two saddle-node ( $SN_2, SN_1$ ) bifurcations. The branch  $e_H$  is stable up to the Hopf bifurcation and becomes unstable afterwards. The branch  $e_M$  is of saddle type while the lower branch  $e_L$  is stable. We extend the Hopf point and obtained a family of unstable limit cycles, which are shown by the red hemisphere on the right of the figure. The Hopf bifurcation is subcritical because the emanating branch of limit cycles is unstable. The family of limit cycles ends in a homoclinic bifurcation (HC) when a cycle collides with a point on the saddle branch  $e_M$ . After the homoclinic bifurcation, the limit cycles cease to exist.

If we refer to the time series in **Figure 2.2(a)**, we see that the silent phase begins when  $Ca$  is large. Therefore, it is more relevant for us to analyse the bifurcation diagram in a backward direction, i.e from right to the left of the diagram. However, prior to any further

analysis, we first compute the eigenvalues of the Jacobian matrix of equation (3) at each equilibrium point. While we already know the stability properties from AUTO, it is useful to know whether the eigenvalues are real or complex. Note that all equilibria in **Figure 2.5** have unique  $V$ -coordinates but not unique  $Ca$ -coordinates. Hence, it is easier to plot the eigenvalues with respect to  $V$  rather than  $Ca$ . **Figure 2.6** shows two separate panels of the real and imaginary parts of the eigenvalues. We treat  $V$  as the independent variable, and plot the corresponding components of the eigenvalues on the y-axis.

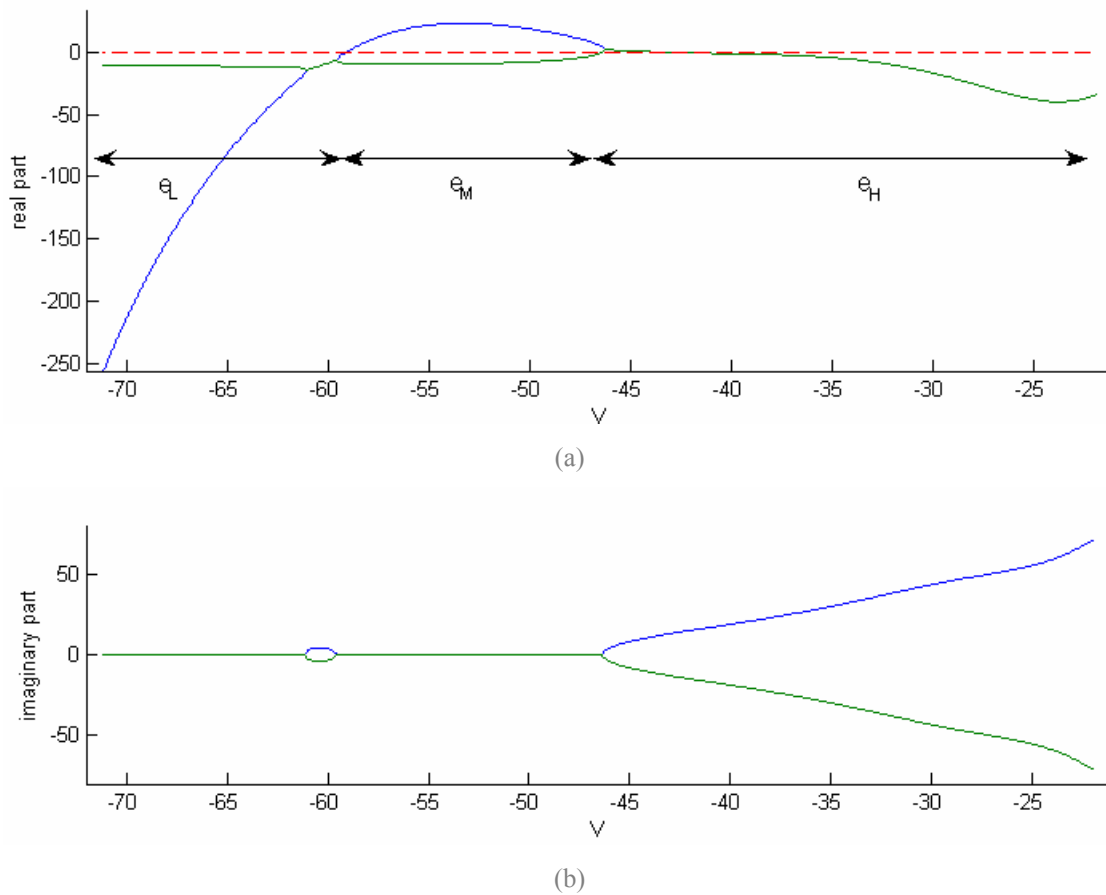


**Figure 2.6** Eigenvalues of the equilibria. The real and imaginary parts are shown on separate panels (a) and (b). Eigenvalues for points on  $e_L$ ,  $e_M$  and  $e_H$  are distinguished by the points where one (real) eigenvalue crosses the x-axis in panel (a).

The equilibria on the branch  $e_H$  are always of spiralling type because the imaginary parts of their eigenvalues are nonzero. Those equilibria are initially stable when the real parts are negative but later become unstable after the real parts cross the x-axis. The eigenvalues of points on the branch  $e_M$  are always real with one branch on the positive and one on the negative side of the y-axis. Thus,  $e_M$  is a branch of saddle points. The stability of points on  $e_L$  varies between a stable node and stable spiral. While the eigenvalues of  $e_L$  always have

negative real parts, the imaginary parts only become nonzero when  $V$  is around  $-60mV$ . Note that towards the left of **Figure 2.6**, branches of the real parts greatly differ in magnitude. This means that the orbit will rapidly decay in one direction of the variable but slowly approaching in the other direction towards the branch  $e_L$  when  $V$  is very negative.

We use the information from the bifurcation diagram in **Figure 2.5** and eigenvalues in **Figure 2.6** to interpret the shape of the global attractor. We know from equation (1) that  $\dot{Ca}$  is negative for low  $V$ , i.e.  $Ca$  decreases, and  $\dot{Ca}$  is positive for high  $V$ , so that the direction for  $V$  reverses. Therefore, we start from a point on the branch  $e_L$  at  $Ca = 1.0\mu M$  and continue in the direction of decreasing  $Ca$ . The cell remains quiescent as it traverses along the branch of stable nodes  $e_L$ . After branch  $e_L$  loses its stability in the saddle-node bifurcation  $SN_1$ , the global attractor jumps to the only remaining branch of attracting equilibria  $e_H$ . This movement initiates the active phase where  $Ca$  starts to increase. Along the path, the imaginary parts of equilibria on the branch  $e_H$  are initially large in magnitude but decrease as  $V$  decreases. Hence, we expect that the global attractor oscillates and traverses around the branch  $e_H$  with some overshoots and increasingly damped oscillations.

**Figure 2.7** visualises the results as we overlay the bifurcation diagram with the periodic attractor. To our surprise, the global attractor spirals below the branch  $e_H$  instead of around it. Furthermore, one would expect that the homoclinic bifurcation plays a role in pushing the global attractor back down. However, the global attractor drops down earlier to  $e_L$ , which terminates the active phase. The two discrepancies of imperfect oscillation below branch  $e_H$  and the earlier termination of the active phase are highlighted in light blue colour. We evaluate these two discrepancies in **Section 2.2.1** and **Section 2.2.2**, respectively.

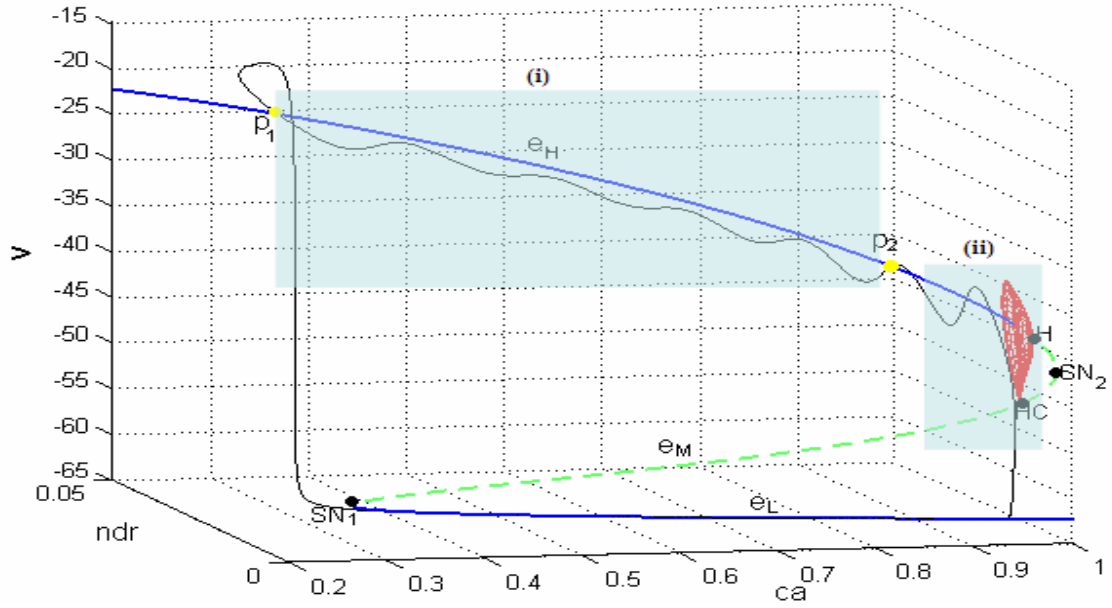


**Figure 2.7** The black curve of the global periodic attractor overlaid on the bifurcation diagram. Segments of discrepancies are highlighted in light blue colour.

### 2.2.1 Oscillations below spiral nodes

From the first discrepancy segment (i) in **Figure 2.7**, we can see the global attractor spirals below  $e_H$  instead of around that attracting branch. There are several reasons to clarify this scenario. The possible main factor is the actual dynamics of  $Ca$ . We also need to take into account the instantaneous position of the spiralling part of the global attractor relative to the branch  $e_H$  and the magnitude of the imaginary eigenvalues for points on  $e_H$ . For investigation, we take two points  $p_1$  and  $p_2$  at the border of segment (i). These points are the yellow dots in **Figure 2.7**. We consider the two cross-sections in the  $(n_{dr}, V)$ -plane at the corresponding  $Ca$ -values for  $p_1$  and  $p_2$ . Imagine that the system is frozen at the points  $p_1$  and  $p_2$  and consider the dynamics in the fast subsystem only. Phase portraits in **Figure 2.8** illustrate the evolution of the orbits in both planes.

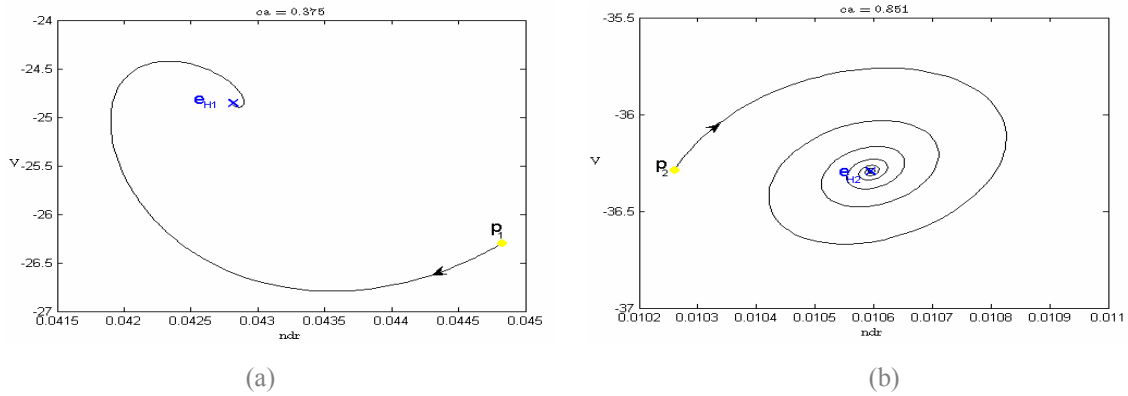


**Figure 2.8** Phase portraits when the system is frozen at  $p_1$  (a) and  $p_2$  (b). Note the different scales on the axes.

We can predict the rate of attraction of the orbit towards  $e_H$  from the imaginary parts of the eigenvalues. For  $Ca \approx 0.375 \mu M$  the magnitude of the imaginary part of points on  $e_H$  is large. Hence for this  $Ca$ -value the orbit spirals very fast towards  $e_H$ , as indicated in **Figure 2.8(a)**. However, before  $p_1$  could flow towards the left of the plane,  $Ca$  has already changed. The orbit then hops to another domain of the fast subsystem. At the same time, the position of equilibria on the branch  $e_H$  also changes. This change causes the global attractor to chase a dynamic equilibrium point. The global attractor manages to overtake the equilibria on the branch  $e_H$  in the  $n_{dr}$ -direction several times, but does not succeed in the  $V$ -direction. **Figure 2.9** shows this act of pursuit in the segment (i) enlarged from **Figure 2.7**, with some additional arrows to show the direction of the global attractor. When  $Ca$  increases to  $0.851 \mu M$ , as shown in **Figure 2.8(b)**, the global attractor is ultimately able to be at about the same level as the point on  $e_H$  in the  $V$ -direction. We then observe that the global attractor spirals perfectly around the branch  $e_H$ .

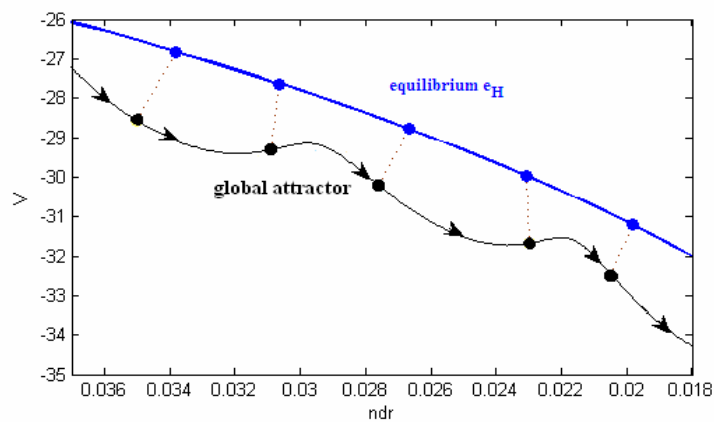


**Figure 2.9** The act of pursuit of the dynamic equilibria on the branch  $e_H$  by the global attractor in the  $(n_{dr}, V)$ -plane.

### 2.2.2 Ending the active phase before the homoclinic bifurcation

**Figure 2.10** shows an enlargement of segment (ii) in **Figure 2.7**. Instead of falling after or near the Hopf region, the global attractor drops down before reaching the homoclinic bifurcation. This behaviour contrasts with the theory, since  $e_H$  is still a branch of stable equilibria at the moment when the global attractor drops down. We believe the departure from the active phase is caused by the invariant stable manifolds of the fast subsystem.

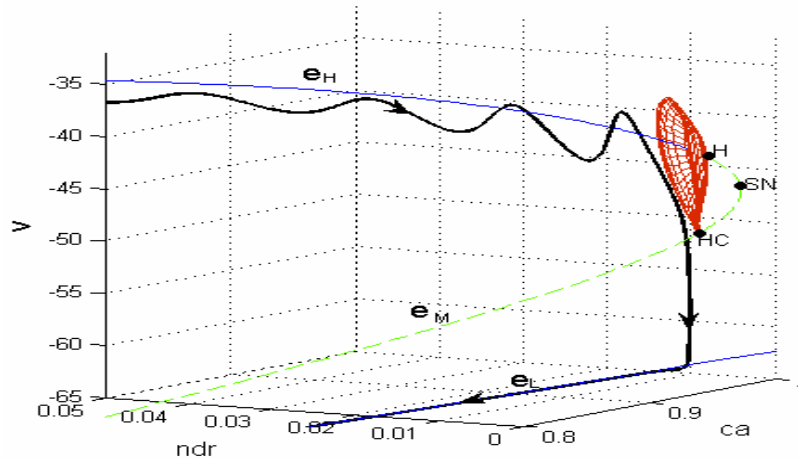


**Figure 2.10** Closer view of the end of the active phase.

### 2.3 Stable manifolds computation

The stable manifolds are associated with the saddle points on the branch  $e_M$  and they are defined as the one-dimensional curves of points that approach  $e_M$  asymptotically as time grows to infinity [13]. These manifolds separate the basins of attraction of the other two stable equilibria that coexist in the fast subsystem. We use XPP to find approximations of the manifolds for each  $Ca$ . In this interface, we initially guess the position of a saddle point based on intersections of the nullclines using a mouse. When the spot is specified as a singular point, XPP then attempts to find the coordinates of the saddle point, and approximates the invariant manifolds of that point. ‘Shoot’ and ‘Backward’ commands are used afterwards. These commands allow XPP to use the coordinates of the saddle point as the initial point and integrate it backward in time. The solution curves represent the invariant stable manifolds of the saddle point on  $e_M$ , denoted as  $W^s(e_M)$ . An example of the manifold approximation is shown in **Figure 2.11** for  $Ca = 0.35 \mu M$ .

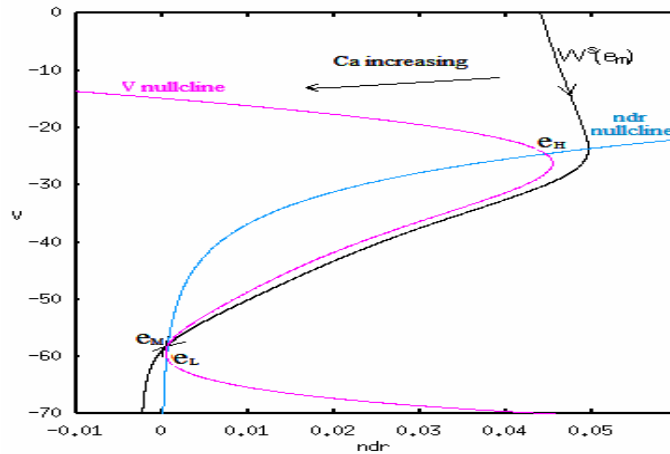


Figure 2.11 Stable manifolds for  $Ca = 0.35 \mu M$ .

The stable manifold consists of two branches. The lower branch emerges from the bottom left side of the  $V$ -nullcline. Another branch decays from a very large  $V$ . The branch crosses the  $n_{dr}$ -nullcline as it declines down the plane. This intersection forces the trajectory to fall and move towards the left of the plane. This branch stays very close to the slope of the  $V$ -nullcline as it approaches the saddle  $e_M$  asymptotically.

The structure in **Figure 2.11** remains virtually the same as  $Ca$  gradually increased to  $0.92929 \mu M$ . After this value there is a sudden and dramatic change in the size of the basin of  $e_H$ . **Figure 2.12** shows this different structure for  $Ca = 0.93 \mu M$ . Although the manifold has shifted to the left, the lower branch has not moved much, but the upper one is qualitatively very different from the situation for  $Ca = 0.35 \mu M$ .

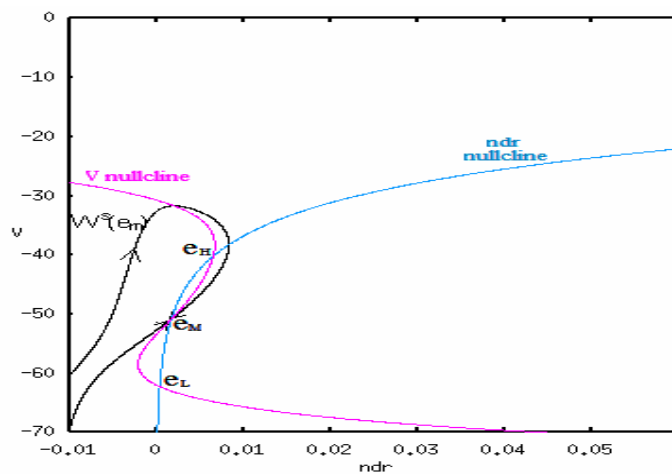
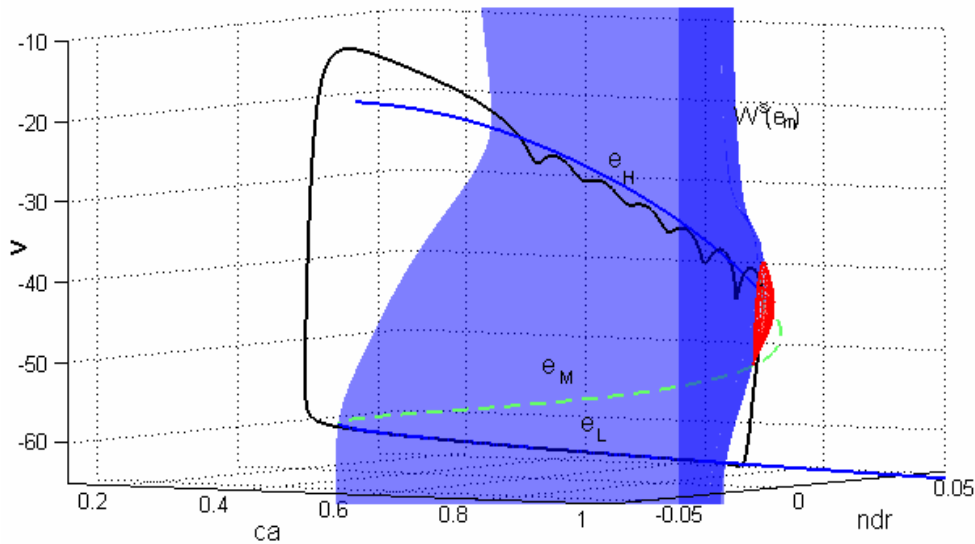


Figure 2.12 Stable manifold of the saddle point for  $Ca = 0.93 \mu M$ .

Instead of growing from the upper part of the plane, the branch now rises from the bottom left corner of the plane. An intuitive explanation of this abrupt change is the idea of a

segment of the upper branch that flows too close to the  $V$ -nullcline. Ultimately, there will be a point when the  $V$ -nullcline and the manifold touch each other. The transition happens very quickly, because the rate at which  $V$  changes is always very fast compared with the change in  $n_{dr}$ . Therefore, the upper branch dramatically drops to the bottom part of the plane after the manifold crosses the nullcline. This transformation, indeed, happens in a  $Ca$ -interval of order of  $10^{-5} \mu M$ .

The final step is to combine the manifold computations into a continuous surface and include it in the bifurcation diagram of **Figure 2.7** along with the global attractor. **Figure 2.13** shows this using a different viewing angle from that in **Figure 2.7**. The manifold surface is rendered transparent, because it partially encloses the global attractor and the bifurcation diagram.



**Figure 2.13** Bifurcation diagram, stable manifolds of the fast subsystem and the global periodic attractor in the phase space. The manifolds are the transparent blue surface; see also **Figure 2.7**.

In the two-dimensional fast subsystem, each manifold is a separatrix between the basins of attraction of the equilibria  $e_H$  and  $e_L$ . An orbit that lies inside the basin of attraction of  $e_H$  can never cross the boundary and get attracted to  $e_L$  [13]. A similar condition applies to orbits in the basin of  $e_L$ . However, this statement is not true for the full system. The dynamics of  $Ca$  allows an orbit to pass through the basin boundary. In fact, for the global attractor, this happens precisely at the end of the active phase. The orbit leaves the basin of attraction of  $e_H$  and escapes to the back side of the manifolds. Because  $Ca$  is still increasing after the global attractor moves through the manifold surface, it can only move

further away from the basin boundary. The global attractor now lies in the basin of attraction of  $e_L$ . Thus, it will converge to  $e_L$  and the active phase ends. **Figure 2.14** illustrates the moment of escape from the basin of attraction of  $e_H$ , which occurs between  $Ca = 0.9293 \mu M$  and  $Ca = 0.9512 \mu M$ .

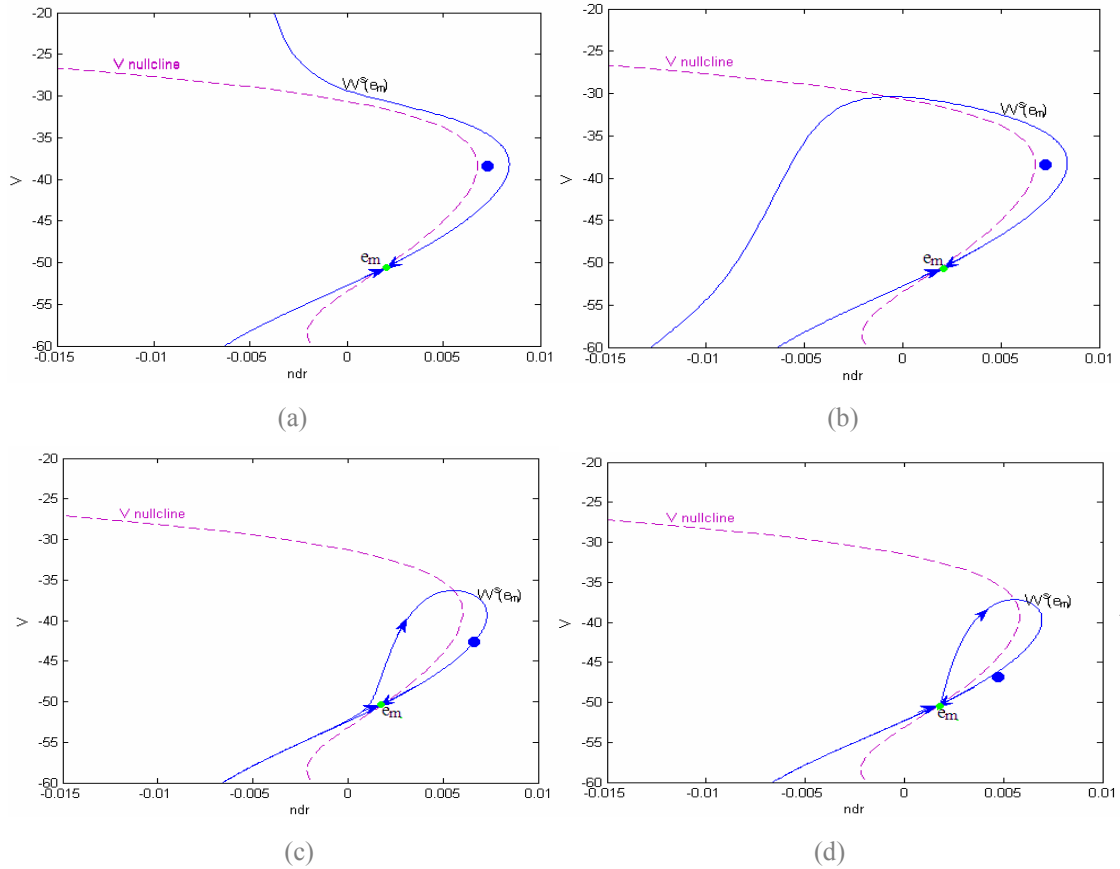


**Figure 2.14** One-dimensional cross-sections from **Figure 2.13** show the sequence of manifold transformations as  $Ca$  increases. The global attractor, indicated by a blue dot in each domain, lies inside the basin of attraction of the point  $e_H$  in panels (a) and (b), but crosses the basin boundary in panel (c); it then moves towards  $e_L$  in panel (d). The  $V$ -nullclines are also shown in the panels.

**Figure 2.14** shows how the upper branch of the stable manifold of  $e_M$  drops and the basin of attraction of  $e_H$  suddenly becomes smaller as  $Ca$  increases. The global attractor continues to spiral within a dynamically changing basin of attraction. In **Figure 2.14(c)** the global attractor lies exactly on the basin boundary and crosses over to the other side into the basin of attraction of  $e_L$ . Therefore, the global attractor is forced to flow towards  $e_L$  and terminate the active phase at a  $Ca$ -value that is lower than expected. An early end of the active phase has also been observed when we have 20% blocked BK-channels in the system and the outcome agrees with our theory of the relationship with the stable manifolds and the termination of the active phase. This case will be further discussed in **Section 4**.

## SECTION 3 PHASE-RESETTING

### 3.1 Definition and procedures

The second part of this project focuses on analysing the stability of the bursting pattern and the system's response to external perturbations. By exerting a perturbation of an electrical current, we may influence the phase of the orbit's eventual periodic motion. This process is known as phase-resetting [8]. We mentioned in **Section 2.1** how an orbit starting from an arbitrary initial condition will eventually settle on a global periodic attractor except for a possible difference in phase. **Figure 3.1(a)** displays a phase change in the  $V$ -coordinate of the orbit when we perturb the system with a current pulse of magnitude 4.8; the pulse is shown in **Figure 3.1(b)**. The current is applied for 0.05s towards the end of the silent phase.

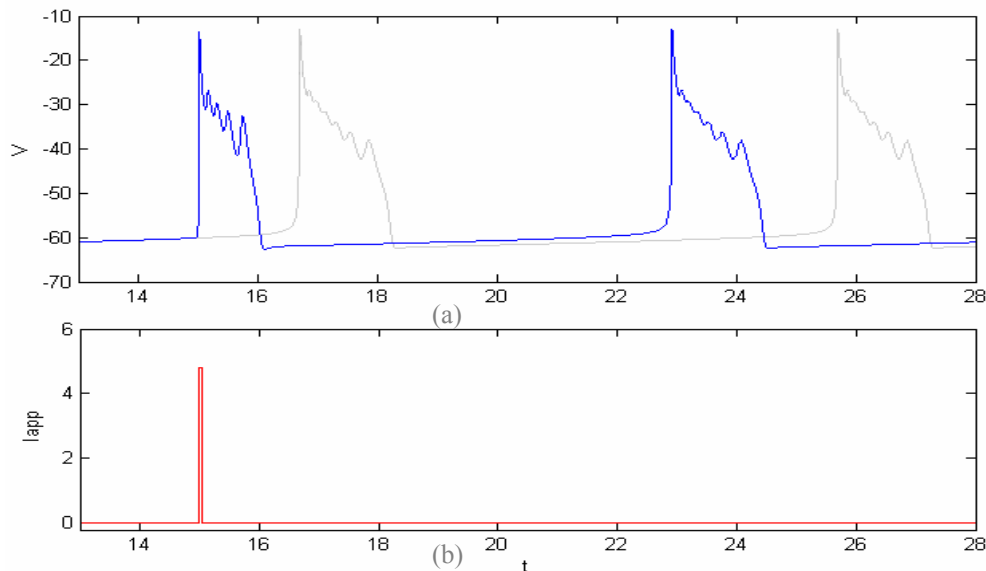


**Figure 3.1** Phase-resetting as a result of a perturbation via the external current. The light-grey and blue curves in panel (a) are the unperturbed and perturbed time series in  $V$ , respectively. Panel (b) shows the brief current input that is applied for 0.05s with strength 4.8.

The applied current advances the phase of the periodic motion because the following burst happens earlier than it would be without any external perturbation. Similarly, we may also delay the phase of the periodic motion, by adjusting the strength of the external current and choosing an appropriate moment in the silent phase. We investigate the influence of the current on the bifurcation structure and verify whether the relationship between the termination of the burst and the stable manifolds of the underlying fast subsystem is still

valid as soon as we turn off the current. We only concentrate on resetting the system from the silent to the active phase.

## 3.2 Resetting in the fast subsystem

### 3.2.1 Properties of the applied current

Let us begin with the phase plane analysis of the fast subsystem for  $Ca = 0.85 \mu M$ . From the bifurcation diagram in **Figure 2.5**, there are three equilibria:  $e_H$  corresponds to the active phase,  $e_L$  to the silent phase and the saddle point  $e_M$  has the stable manifold  $W^S(e_M)$  that forms the basin boundary between the basins of attraction of  $e_H$  and  $e_L$ . We use the silent phase  $e_L$  as the initial condition. We turn on the applied current  $I_{app}$  in equation (3) and maintain the current until the end of the simulations. The strength of  $I_{app}$  for each solution differs by 0.001 from 0 to 200. We plot the perturbed solutions correspond to each  $I_{app}$  in a single phase portrait, as illustrated in **Figure 3.2**.

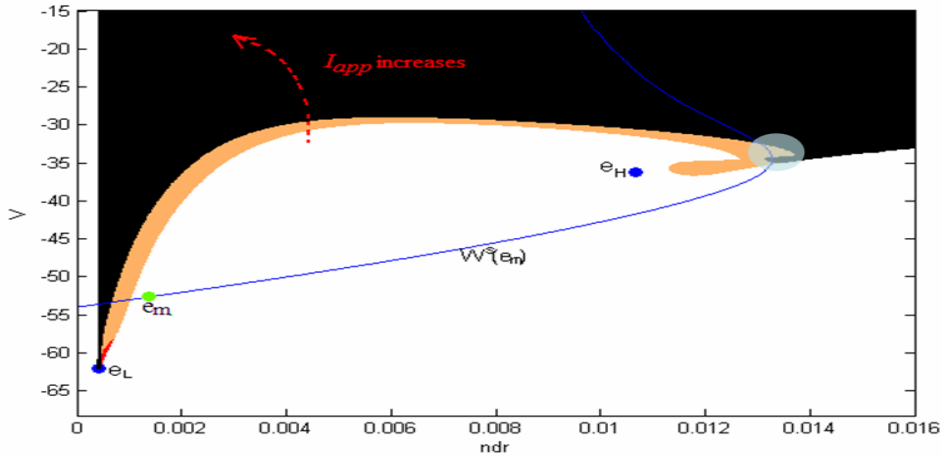


**Figure 3.2** Phase portrait of the fast subsystem for  $Ca=0.85 \mu M$ , with  $I_{app}$  ranging from 0 to 200.

The behaviour of the orbits is labelled by colour. The small red region near  $e_L$  is the collection of the orbits with  $I_{app}$  of strength between  $0 < I_{app} \leq 0.192$ . The orbits converge from the initial point  $e_L$  to perturbed equilibria below the basin boundary. Such strengths of  $I_{app}$  are too weak to push the system from the silent to the active phase and the orbits with these strength will return to  $e_L$  as soon as the effect of  $I_{app}$  is removed. For magnitudes of  $I_{app}$  between  $0.193 \leq I_{app} \leq 0.479$  we obtain orbits that cross the basin boundary from  $e_L$  and converge to perturbed equilibria that are close to  $e_H$ . These orbits

are coloured orange. Each increase in the strength of  $I_{app}$  causes the perturbed equilibrium point to move closer to the basin boundary of  $e_H$ . When  $I_{app} = 0.479$ , the domain has a perturbed equilibrium point that lies approximately on the basin boundary. Resetting the system with a strength slightly less than the upper limit  $I_{app} = 0.479$  may result in a success or failure as the orbit moves transiently in and out of the basin boundary of  $e_H$  for such  $I_{app}$ . The transient motions are highlighted with a blue light circle. Any strength of  $I_{app}$  larger than 0.479 drives the orbit outside the basin of attraction of  $e_H$ . The orbits for this case are coloured black. We will have a minimum and maximum duration of the pulse  $I_{app}$  so that the orbits are not outside the basin of attraction of  $e_H$  when  $I_{app}$  is turned off. For  $I_{app}$  slightly larger than the lower limit  $I_{app} = 0.479$ , the orbits also transiently spiral in and out of the basin of attraction of  $e_H$  and for these orbits, there will be several additional time intervals at which we may turn off the current so that the orbits converge to  $e_H$ .

### 3.2.2 Change in the bifurcation structure

We now study in more detail how  $I_{app}$  alters the bifurcation diagram of the fast subsystem.

**Figure 3.3(a)** illustrates the bifurcation curve in the  $(Ca, V)$ -space when we apply  $I_{app}$  of strength 0.193. We include the unperturbed bifurcation diagram with  $I_{app} = 0$  in light grey for comparison.

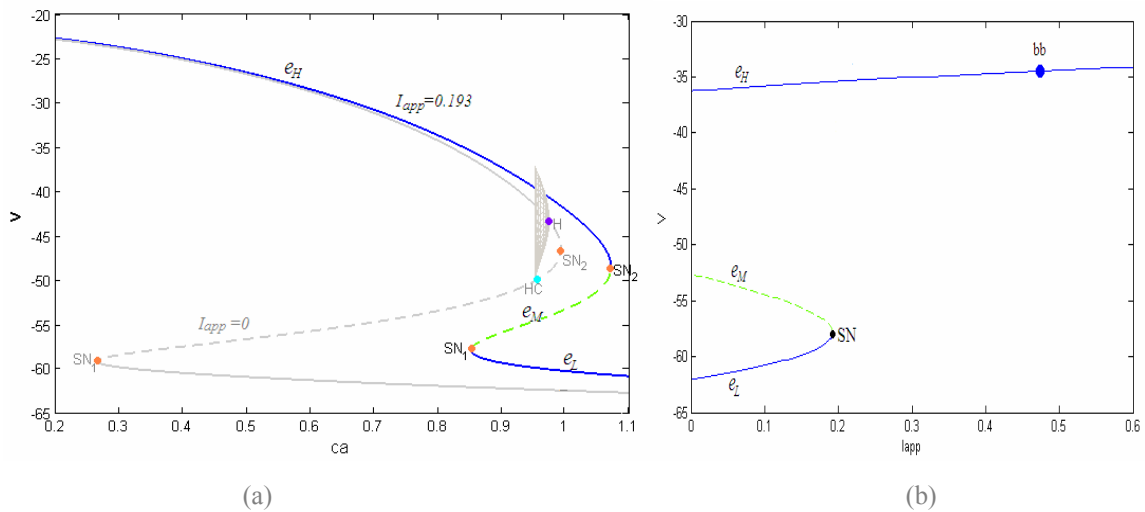


**Figure 3.3** (a) The bifurcation diagrams of the fast subsystem with  $I_{app} = 0$  and  $I_{app} = 0.193$ . (b) The bifurcation diagram with  $I_{app}$  as the bifurcation parameter for domain  $Ca = 0.85 \mu M$ .

From **Figure 3.3(a)**, we see that the change in  $I_{app}$  exerts a much greater effect in shifting  $SN_1$  compared to  $SN_2$ , while causing the Hopf and homoclinic bifurcation points to disappear from the bifurcation curve. If we reset the system during the silent phase with  $I_{app}$  of strength 0.193 such that the orbit is to the left of the point  $SN_1$  of the perturbed system, the orbit will only jump from the bottom solid grey line to the points on the blue branch  $e_L$  in **Figure 3.3(a)**. The orbit continues to traverse along this branch until it reaches point  $SN_1$  of the perturbed curve at  $Ca \approx 0.85$ , and jumps to the remaining perturbed branch of attracting equilibria  $e_H$  to initiate the active phase. Thus, if we want to reset the system from the silent to the active phase at a particular  $Ca$ -value, we have to apply  $I_{app}$  such that the current is able to push  $SN_1$  beyond that value of  $Ca$ .

The analysis with the phase portrait in **Figure 3.2** suggests that the strength of  $I_{app}$  must be sufficiently large to drive the orbit beyond the basin boundary. At the same time, the strength must not be too strong as it may drive the orbit outside the basin of attraction of  $e_H$ . The upper and lower limits of such strengths are given by the upper and lower limits of  $I_{app}$  corresponding to the orbits in the orange region in **Figure 3.2**. As an alternative, these limits can be determined more conveniently from a bifurcation diagram with  $I_{app}$  as a bifurcation parameter. **Figure 3.3(b)** shows this bifurcation diagram for  $Ca = 0.85 \mu M$ , where the  $V$ -coordinate of the perturbed equilibria is plotted as a function of  $I_{app}$ . The curves  $e_L$ ,  $e_M$  and  $e_H$  are now the branches of equilibria obtained when we turn on  $I_{app}$ . As before,  $e_L$  and  $e_H$  are the branches of attracting equilibria while  $e_M$  is the branch of saddle points. The intersections of these curves with the  $V$ -axis give the  $V$ -coordinates of the equilibria with  $I_{app} = 0$ . As  $I_{app}$  increases,  $e_L$  and  $e_M$  extend and meet at a saddle-node bifurcation SN; this happens at  $I_{app} = I_{app,SN} \approx 0.192$ . If  $I_{app}$  is of strength  $I_{app} \leq I_{app,SN}$ , an orbit starting from the equilibrium point  $e_L(0)$  will only converge to an equilibrium below the basin of attraction of  $e_H(0)$ . When  $I_{app} > I_{app,SN}$ , only the branch  $e_H$  of attracting equilibria exists. Hence, the orbit will converge to  $e_H$  when we apply  $I_{app}$  of such strength. The lower limit of strength  $I_{app}$  to drive the orbit across the basin boundary is therefore given by  $I_{app,SN}$ . To find the upper limit of  $I_{app}$  such that the equilibria on branch  $e_H$  still lie inside the basin of attraction of  $e_H(0)$ , we locate the intersection point between  $e_H$  and

the stable manifold  $W^s(e_M)$  in **Figure 3.2**. This intersection point is the equilibrium point on  $e_H$  that sits approximately on the basin boundary, with its  $V$ -coordinate indicated by the black dot labeled ‘bb’ in **Figure 3.3(b)**. The corresponding strength  $I_{app} \approx 0.49$  is the maximum strength of  $I_{app}$  to ensure that the orbits do not converge to a point outside the basin of attraction of  $e_H(0)$ .

For smaller  $Ca$ -values, the branches  $e_L$  and  $e_M$  in **Figure 3.3(b)** will be pulled towards the  $V$ -axis and  $I_{app,SN}$  is smaller. Hence, the lower limit of  $I_{app}$  is smaller. The upper branch  $e_H$  is still approximately a straight line with the point bb shifted towards the direction of increasing  $I_{app}$ . This results in a higher upper limit for  $I_{app}$  for which the perturbed equilibria still lie inside the basin of attraction of  $e_H(0)$ . As points SN and bb move further apart from each other in the horizontal direction, the difference between the lower and upper limit of  $I_{app}$  increases.

Another type of bifurcation diagram that may give us information on the strength of  $I_{app}$  is the two-parameter bifurcation diagram. This is shown in **Figure 3.4**. We can determine how small the lower limit of strength  $I_{app}$  is for arbitrary choices of  $Ca$  by locating the  $(I_{app}, Ca)$ -coordinates on the branch of  $SN_1$  in this diagram.

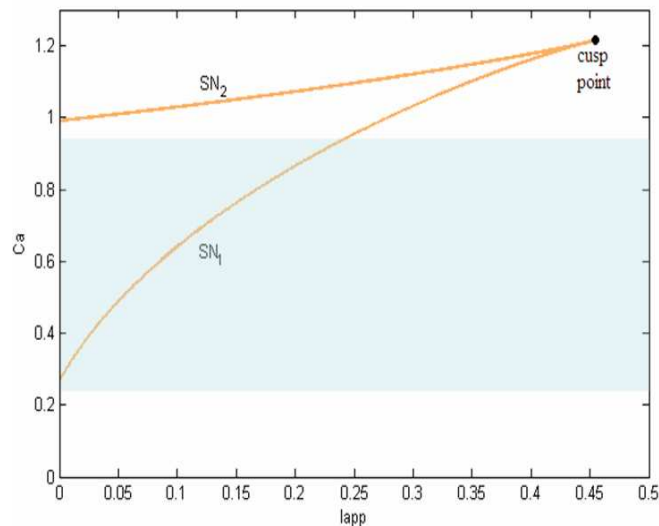


**Figure 3.4** The branches of saddle-node bifurcation points in the two-parameter bifurcation diagram. The light blue segment is the domain associated with the silent phase.

Recall from **Figure 2.5** that there are two saddle-node bifurcations  $SN_1$  and  $SN_2$  for the unperturbed fast subsystem. The two-parameter bifurcation diagram in **Figure 3.4** shows how these two bifurcation points depend on  $I_{app}$ . We run AUTO for forward continuation in  $I_{app}$  starting from  $SN_1$  at  $I_{app} = 0$ . AUTO traces the branch of  $SN_1$  and stops momentarily at the cusp point (black dot) before tracing the branch of  $SN_2$  in a backward direction. We are only concerned with the branch of  $SN_1$  as the coordinates given by this branch are those that specifying the lower limit  $I_{app,SN}$  to drive the orbit successfully across the basin boundary. The relevant range of  $Ca$ -values that cover the silent phase is indicated by the light-blue segment. For the domains with  $Ca$  approximately larger than  $1.2\mu M$ , there is only one branch of attracting equilibria after  $e_L$  and  $e_H$  merge in the cusp point. Hence, there will be no lower limit for  $I_{app}$  to reset the system into the active phase for  $Ca \geq 1.2\mu M$ , approximately. However, these are not the domains associated with the silent phase because  $Ca$  only varies between approximately  $0.2 \leq Ca \leq 0.95$  during the silent phase; see also **Figure 2.2(a)**.

We include the branches of Hopf and homoclinic bifurcations in the two-parameter bifurcation diagram in **Figure 3.5(a)**. In the figure, we can see that the Hopf and homoclinic points on the respective violet and light blue lines move together towards the

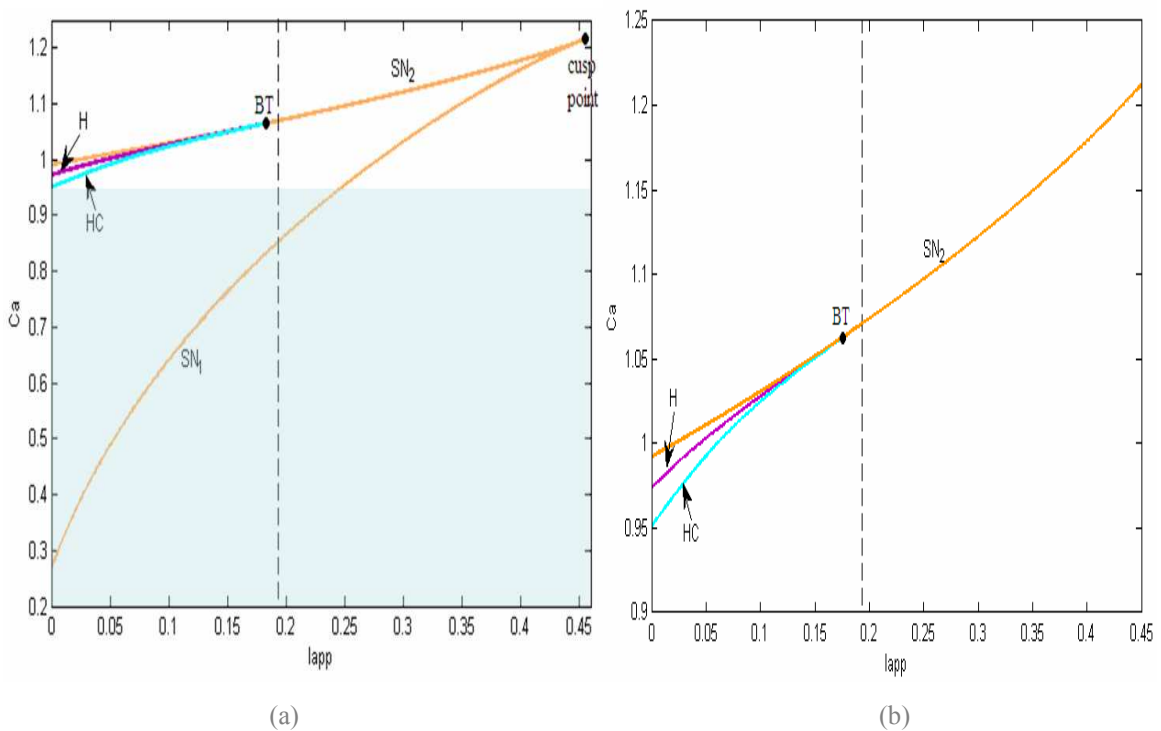


**Figure 3.5** (a) The two-parameter bifurcation diagram shows branches of the bifurcation points. Panel (b) shows an enlargement.

branch of  $SN_2$  as  $I_{app}$  increases. These three bifurcation branches meet at a Bogdanov-Takens (BT) bifurcation point [9]; see also the enlargement in **Figure 3.5(b)**. The branches that intersect with the dotted line are the bifurcation points that exist when  $I_{app}$  of strength 0.193 is applied. As we can see from this figure, the case for  $I_{app} = 0.193$  lies to the right of BT point, so that no other bifurcation points are expected apart from the two saddle-node bifurcations  $SN_1$  and  $SN_2$ . We are not concerned with the influence of the Hopf and homoclinic bifurcation in the transition of the phase since the two-parameter bifurcation diagram in **Figure 3.5(a)** shows that these points will move away from the domain of interest as soon as we turn on the current.

### 3.2.3 Duration to reach the basin boundary

If we apply the current with the minimum strength  $I_{app,SN}$ , it may take a long time for the orbit with such strength to move across the basin boundary. To analyse this, we refer again to the bifurcation diagram in **Figure 3.3(b)** for  $Ca = 0.85\mu M$ ; an enlargement is shown in **Figure 3.6**.

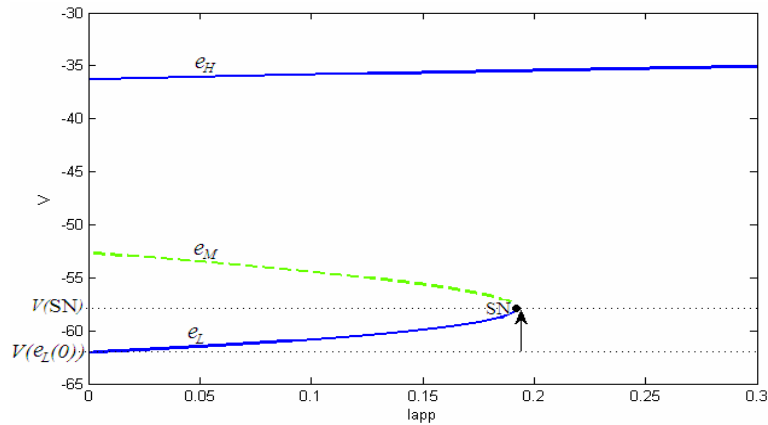


**Figure 3.6** The left-half plane of **Figure 3.3 (b)**. The arrow indicates the direction of the orbit that attempts to pass very close to SN towards the basin boundary of  $e_M(0)$  with the minimum strength of current  $I_{app,SN}$ .

To approximate the minimum duration  $t_{min}$  for the orbit to cross the basin boundary with the current of strength  $I_{app,SN}$ , we first consider a topological normal form of a saddle-node bifurcation. The normal form for the SN point in **Figure 3.6** is given by

$$\dot{y} = y^2 + \lambda . \tag{4}$$

This equation generally describes the dynamics in a small neighbourhood of a saddle-node bifurcation point. It gives two equilibria  $y_{1,2} = \pm\sqrt{-\lambda}$  for  $\lambda < 0$  and no equilibria for  $\lambda > 0$ . The saddle-node bifurcation happens at the point when  $\lambda = 0$ , i.e., at  $y = 0$ . The variable  $y$  and the constant  $\lambda$  are equivalent to

$$\begin{aligned} y &= V - V(SN), \\ \lambda &= I_{app} - I_{app,SN}. \end{aligned} \quad (5)$$

We are interested in the domain specified by  $V \geq V(e_L(0))$  and  $I_{app} > I_{app,SN}$ . There are no real equilibria in this domain since it corresponds to the domain on the right hand side of SN point. We integrate equation (4) to find the solution as

$$\begin{aligned} \int \frac{dy}{y^2 + \lambda} &= \int dt \Leftrightarrow \\ y(t) &= \sqrt{\lambda} \tan\{\sqrt{\lambda}(t + const)\}. \end{aligned} \quad (6)$$

We then use equation (5) and initial condition  $V = V(SN)$  at time  $t = 0$  to obtain the expression of time  $t$  as

$$t = \frac{1}{\sqrt{I_{app} - I_{app,SN}}} \tan^{-1}\left(\frac{V - V(SN)}{\sqrt{I_{app} - I_{app,SN}}}\right) \quad (7)$$

for an arbitrary  $V$ -coordinate. The constant term in equation (6) vanishes since we use the SN point as the initial condition. In fact, we would like to take the lower equilibrium point  $e_L(0)$  as the initial state, but this leads to a very large difference between the numerical value of  $t_{\min}$  obtained by simulation and the  $t_{\min}$  given by equation (7) for  $I_{app,SN}$  because point  $e_L(0)$  is too far away from SN. Our approximation using the normal form in equation (4) is only accurate for points in a small neighbourhood of SN. We find the time  $t_{\min}$  as the time it takes the orbit to move from  $V(SN)$  to  $V(SN) + \delta V$ . We substitute these two  $V$ -values into equation (7) to get

$$t_{\min} = \frac{1}{\sqrt{I_{app} - I_{app,SN}}} \tan^{-1} \left( \frac{\delta V}{\sqrt{I_{app} - I_{app,SN}}} \right) \quad (8)$$

Observe that in the limit  $I_{app} \rightarrow I_{app,SN}$ , the minimum time  $t_{\min}$  for the orbit to pass the SN point on its way to the basin boundary tends to infinity. Based on this argument, we may deduce that it takes an increasingly longer time for the orbit to cross the basin boundary for the strength of  $I_{app}$  just larger but increasingly closer to  $I_{app,SN}$ .

**Figure 3.7** shows a simulation of equation (3) with  $Ca = 0.85 \mu M$  where we integrate the initial condition  $e_L(0)$  for varying  $I_{app}$  and measure the time it takes to reach the basin boundary. Note that the data appears to have a vertical asymptote; this is because  $I_{app} \approx 0.192$  is the minimum strength required to pass into the basin of  $e_H$ . **Figure 3.8** shows equation (8) for values  $\delta V = 0.1$ ,  $\delta V = 0.01$  and  $\delta V = 0.001$ . The numerical data in **Figure 3.7** lies practically on top of the red curve for  $\delta V = 0.01$  in **Figure 3.8**. Hence, despite the fact that the normal form only applies in a small neighbourhood of the saddle-node bifurcation in **Figure 3.6**, it seems that we can use equation (8) as a function for the minimum duration  $t_{\min}$  over the whole range of  $I_{app}$  if we choose  $\delta V$  appropriately.

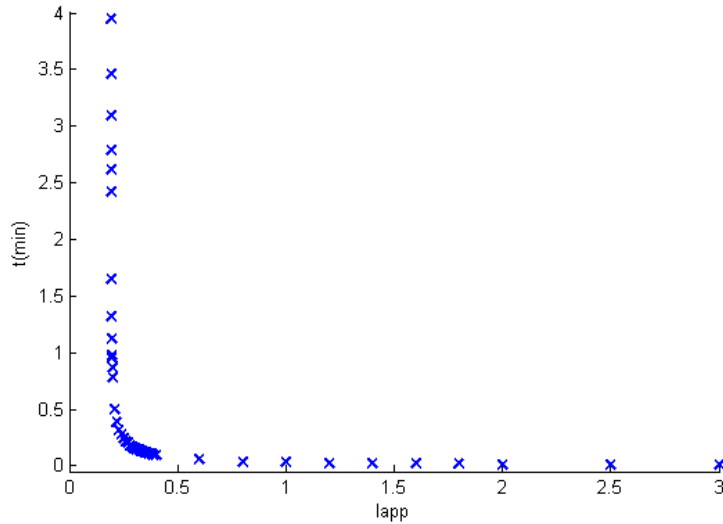


**Figure 3.7** The numerical data of minimum time  $t_{\min}$  for different values of  $I_{app}$ .

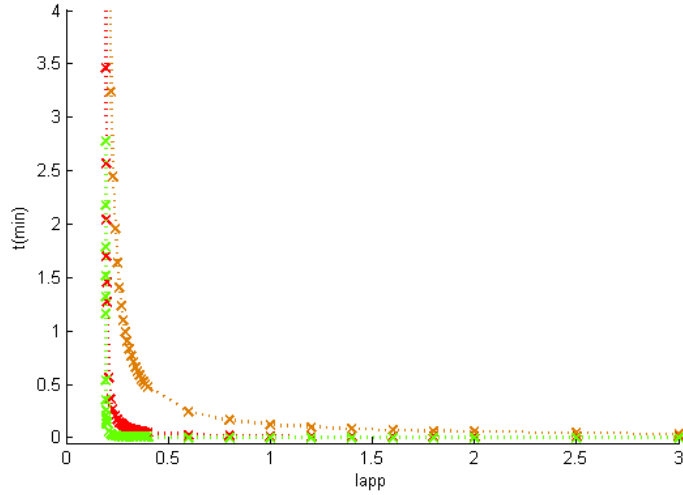


**Figure 3.8** The minimum time  $t_{min}$  approximated from equation (8) for  $dV = 0.1$  (brown),  $0.01$  (red) and  $0.001$  (green) for similar values of  $I_{app}$  in **Figure 3.7**.

### 3.3 Dynamic resetting in the full system

We outline several conditions to reset the system dynamically from the silent to the active phase based on the investigations in the fast subsystem. The analysis in **Section 3.2.2** gives a lower strength of  $I_{app}$  to reset the system for smaller  $Ca$ -values, i.e., less force from  $I_{app}$  to drive the orbit across the basin boundary when the reset occurs relatively late in the silent phase. Moreover, the strength interval of  $I_{app}$  to ensure that the perturbed branch  $e_H$  still lies inside the basin of attraction of  $e_H(0)$  is larger for smaller  $Ca$ -values. This indicates that there is a larger basin for the orbit to land on.

To reset the full system from the silent phase, we expect that there is a particular interval of duration  $\delta t$  to maintain  $I_{app}$  such that the upward resetting results in a prolonged active phase. Otherwise, the reset only results in a short pulse of burst. Significantly, the duration  $\delta t$  where  $I_{app}$  is turned on should not alter the process of terminating the active phase by the stable manifolds of the underlying fast subsystem. **Figure 3.9** illustrates the duration  $\delta w$  of the active phase after a reset of fixed strength and varying  $0 < \delta t \leq 0.5$ . We choose  $Ca = 0.85 \mu M$  and  $Ca = 0.5 \mu M$  that correspond to an early and intermediate resetting in the silent phase; the strength of  $I_{app}$  is  $0.4$  and  $0.5$ , respectively. After we turn off  $I_{app}$ , we measure the time  $\delta w$  for the orbit to spiral around the upper branch of equilibria  $e_H$  until

the instant when the  $V$ -value of the orbit drops below  $-55\text{ mV}$ . In comparison, we record the duration  $\delta w$  of the unperturbed active phase measured from the same phase angle where the current is turned off until the  $V$ -value drops to  $-55\text{ mV}$  as well.

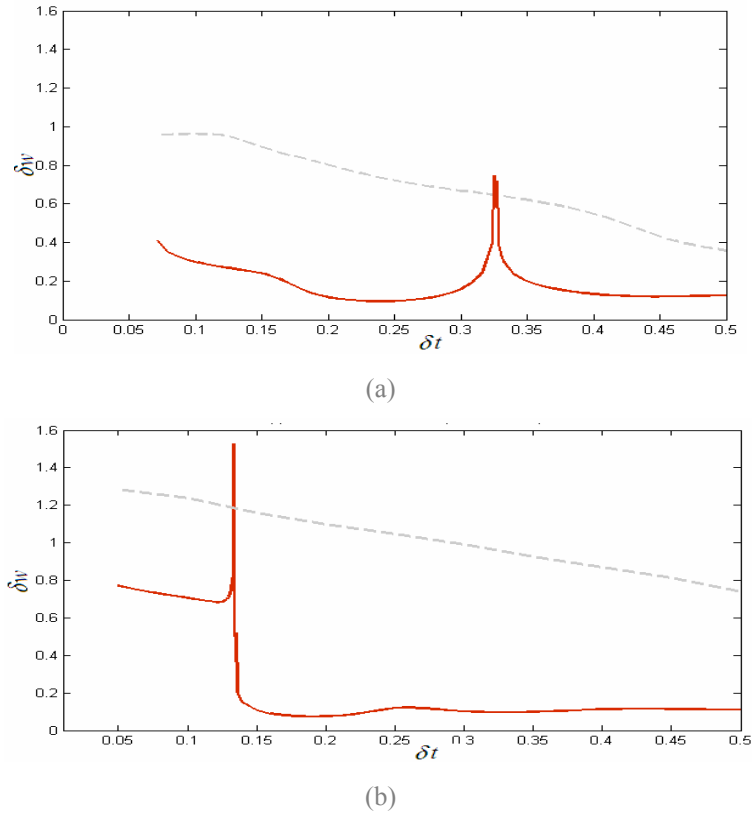


**Figure 3.9** The red curves give the duration  $\delta w$  for the perturbed active phase. Panel (a) shows an early resetting with  $(Ca, I_{app}) = (0.85\mu M, 0.4)$  and panel (b) an intermediate resetting with  $(Ca, I_{app}) = (0.5\mu M, 0.5)$ .

When we apply a current of strength 0.4 at  $Ca = 0.85\mu M$  in the silent phase, the small peak in **Figure 3.9(a)** indicates that  $I_{app}$  manages to land the orbit inside the basin of attraction of unperturbed  $e_H$  when  $\delta t$  is about 0.325s. If we maintain  $I_{app}$  shorter or longer than this, the orbit is either still below the basin of attraction of unperturbed  $e_H$  or already moves outside that basin. The orbit also stays up longer than the unperturbed cycle for such amounts of  $I_{app}$ . In comparison, **Figure 3.9(b)** shows  $\delta w$  for the case of resetting the system in the middle of the silent phase, where  $Ca = 0.5\mu M$  and  $I_{app}$  is of strength 0.5. The current  $I_{app}$  maintained between an approximate range of  $0.05s \leq \delta t \leq 0.13s$  gives an upward resetting with a prolonged active phase. The reset that occurs in the middle of the silent phase has a peak where the orbit stays up much longer. For  $Ca=0.5\mu M$  and  $I_{app} = 0.5$ , this happens when  $I_{app}$  is maintained for about 0.13s .

We take the properties of  $I_{app}$  at the two peaks in **Figure 3.9** and visualise the evolutions of the corresponding perturbed orbits in the state space around the stable manifolds of the unperturbed system in **Figure 3.10**.

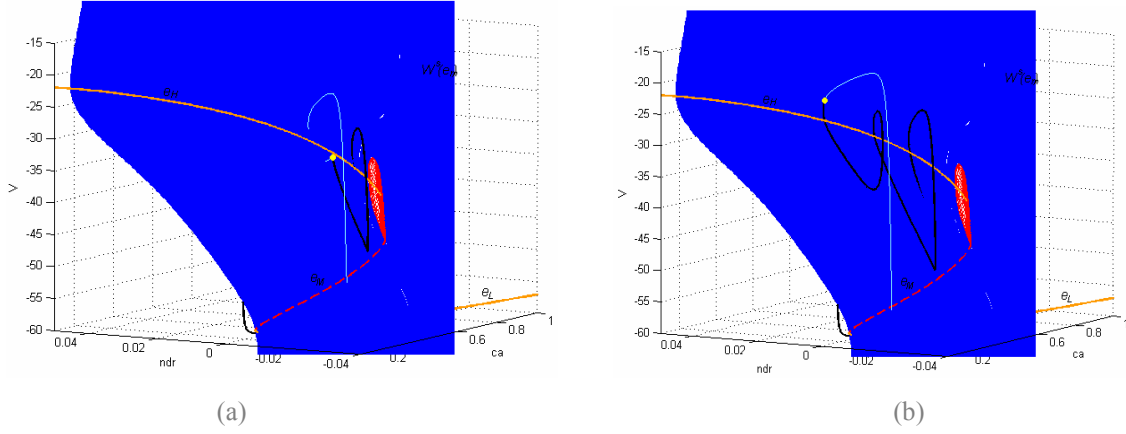


**Figure 3.10** The visualisation of the perturbed orbits that stay up longer than the unperturbed one in the active phase. Panel (a) and panel (b) correspond to the respective resets in the early and middle of the silent phase. The light-grey curves indicate the motions of the orbits when  $I_{app}$  is turned on until this current is removed at the yellow dots.

**Figure 3.10(a)** shows the perturbed orbit with  $I_{app} = 0.4$  that transiently spirals in and out of the basin of attraction of the unperturbed  $e_H$  under the influence of  $I_{app}$ . The orbit is inside the basin when we maintain  $I_{app}$  for 0.325s. The variable  $Ca$  varies slowly towards the end of the active phase and the deformation of the basin of attraction of the unperturbed  $e_H$  also happens rather slowly. If we turn off  $I_{app}$  when the orbit is in this region then it spirals down towards the saddle branch  $e_M$  while creating a loop. As the orbit moves towards the basin boundary,  $Ca$  deforms the basin and causes the orbit to move outside the basin of attraction of the unperturbed  $e_H$ .

**Figure 3.10(b)** shows another reset that results in a perturbed active phase that lasts longer than the unperturbed one. This occurs for the reset with  $I_{app}$  of strength 0.5 approximately in the middle of the silent phase with  $Ca = 0.5 \mu M$ . This current is maintained for 0.133s. After we turn off  $I_{app}$ , the orbit creates loops of increasing amplitude towards the saddle branch  $e_M$ . Again, the orbit spirals very close to the basin boundary since  $Ca$  varies very slowly as well. The orbit stays inside the basin for a relatively long time before it crosses the basin boundary and drops down. For both cases of resetting, we can see that

the termination of the active phase is still governed by the structure of the stable manifolds that defines the basin boundary.

## SECTION 4 ROLE OF THE STABLE MANIFOLDS

In **Section 2**, we established a close relationship between the earlier termination of the active phase and the stable manifolds of the fast subsystem. The results from phase-resetting in **Section 3** are also consistent with this relationship. We now investigate how much the stable manifolds depends on the system parameters. In particular, we return to the full system (and the fast subsystem) with zero  $I_{app}$ , and consider the case when the BK-channels in equation (1) and (3) are blocked by 20%. This means that the parameter  $bblock = 0.2$ ; see the **Appendix** for details. We repeat the construction of the bifurcation diagram and the stable manifolds as in **Section 2**. **Figure 4.1** shows the bifurcation diagrams of the fast subsystem and the global periodic attractors both with 0% and 20% blocked BK-channels in panels (a) and (b), respectively.

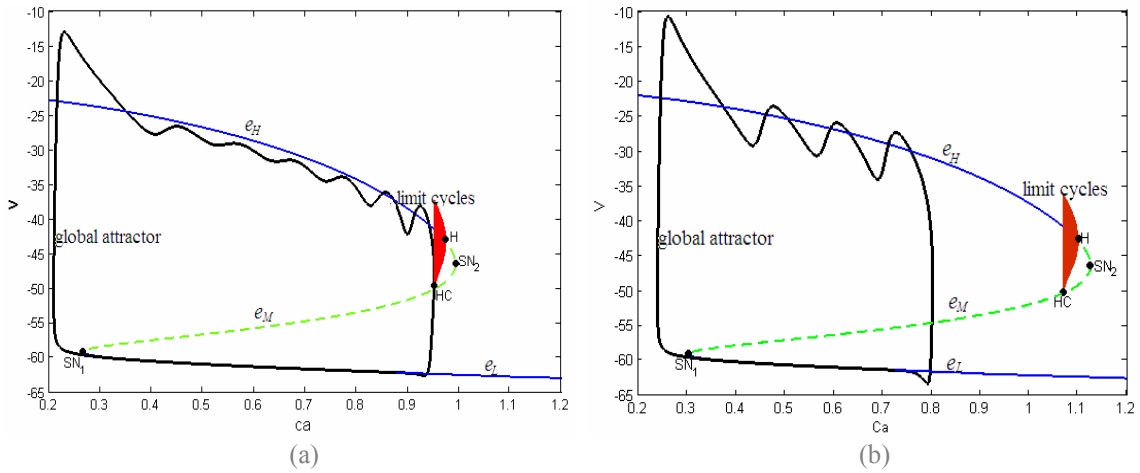


**Figure 4.1** The global periodic attractors and the bifurcation structures in  $(Ca, V)$ -space with (a) 0% and (b) 20% blocked BK-channels.

As shown in the figure, all branches of equilibria in **Figure 4.1(a)** persist in **Figure 4.1(b)**, but the bifurcation curve stretches further to the right of the  $(Ca, V)$ -space and causes the limit cycles to shift in the same direction. Furthermore, note that the global periodic attractor in **Figure 4.1(b)** has fewer and much taller spikes that spiral around the branch  $e_H$  instead of below it. More notably, the global periodic attractor only spirals half-way through  $e_H$  up to approximately  $Ca = 0.8 \mu M$  and falls down much earlier to the branch  $e_L$  than the bursting orbit without blocked BK-channels.

Despite the much earlier termination of the active phase, the dynamics of the global attractor is still determined by the associated basin boundaries of the underlying fast subsystem. **Figure 4.2** shows two different view points of how the global attractor intersects with the basin boundary.

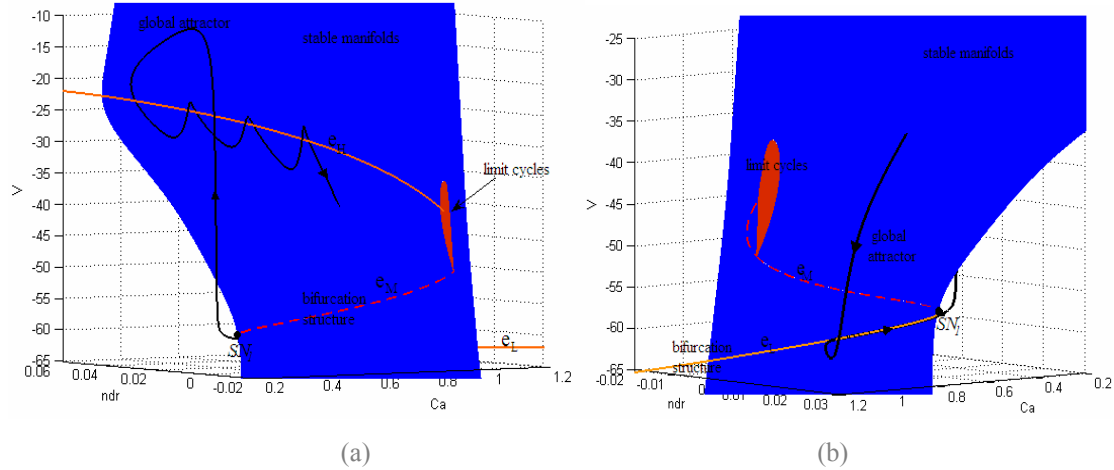


**Figure 4.2** The stable manifolds and global periodic attractor with 20% blocked BK-channels. Both branches of  $e_L$  and  $e_H$  are rendered in orange. The arrows indicate the direction of the global periodic orbit with respect to time.

**Figure 4.2(a)** shows the segment of the global periodic attractor inside the basin of attraction of  $e_H$ . The global attractor enters the basin of attraction of  $e_H$  after it passes through  $SN_1$  on the left end of the red dotted line. The global attractor makes several loops around  $e_H$  and crosses the basin boundary half way along this branch. **Figure 4.2(b)** shows the other segment of the global attractor that lies outside the basin of attraction of  $e_H$ . After the global attractor moves across the basin boundary, it plunges to the right in positive  $n_{dr}$ -direction towards the branch  $e_L$ .

We can see that all ingredients are still important in determining the end of the active phase in terms of the termination of the active phase, even when the BK-channels are partially blocked. We expect similar behaviour of the system when we perturb the system via the external current  $I_{app}$ . To predict the behaviour of the global attractor when we turn on  $I_{app}$ , we produce a two-parameter bifurcation diagram for this system of blocked BK-channels. We obtain a qualitatively similar diagram in comparison with the system without blocked BK-channels; compare also **Figure 3.5(a)**.

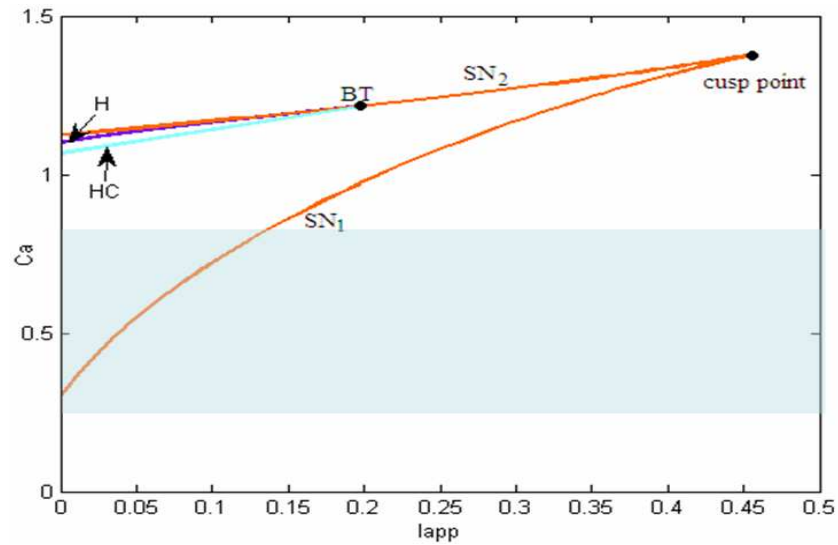


**Figure 4.3** The two-parameter bifurcation diagram with 20% blocked BK-channels. The light blue segment defines the domain associated with the silent phase.

Again, the branches of Hopf and homoclinic bifurcation points move away from the domain of the silent phase as we turn on  $I_{app}$ . Hence, we expect that these bifurcations play no role for the perturbed system with blocked BK-channels. Hence, termination of the active phase when the perturbed orbit crosses the basin boundary is still valid regardless of whether the BK-channels are blocked or not.

## SECTION 5 DISCUSSION AND CONCLUSION

We considered the dynamics and bursting behaviour of somatotroph cells. To this end, we studied a mathematical model involving three variables, namely membrane potential ( $V$ ), calcium ( $Ca$ ) and fraction of the open potassium-channel ( $n_{dr}$ ). We assume that  $Ca$  evolves much slower than  $V$  and  $n_{dr}$ . The mathematical model has a global attractor that corresponds to the bursting behaviour of the cells. The structure of the global attractor is formed by its local behaviour near the equilibria of the underlying fast subsystem. The transition between the silent and the active phase in cells occurs when the global attractor alternately jumps between a branch of stable nodes to another branch consists of spiral equilibria. While the transition from the silent to the active phase can be explicitly explained by the theory of a saddle-node bifurcation, the existing bifurcation structure does not provide an answer on the earlier transition of the cells from the active to the silent phase. We demonstrate how an explanation on the scenario of the earlier termination in the active phase is actually provided by the geometrical structure of the stable manifolds of saddle equilibria in the underlying fast subsystem. Each stable manifold forms the basin boundary between two attracting equilibria in the fast subsystem for a fixed value of  $Ca$ . We observe how the active phase always terminates as soon as the global attractor crosses the stable manifolds of the saddle equilibria.

The bifurcation structure and the stable manifolds of the fast subsystem turned out to be useful when we later study effect from an external perturbation that aims to reset the phase of the system. While we cannot deduce the quantitative amount on the change in phase from these two mechanisms, we can approximate the amount of external electrical current required to bring the system from the silent phase into the active bursting phase from the resetting analysis in the fast subsystem,. Namely, in the fast subsystem, such a change comes about when the perturbation is strong enough to bring the orbit inside the basin of the upper attracting equilibrium. This can be defined as the value that causes a saddle-node bifurcation. By using the topological normal form equation, we show that although such strength is able to drive the orbit across the basin boundary, the time it takes to do so will be infinitely long.

In the dynamic resetting, the average time to maintain the current such that the current can bring the system into the active bursting phase decreases if the reset occurs relatively late in the silent phase. For any phase angle that associated with the silent phase, there is a

particular duration to hold the current so that the perturbed active phase lasts longer than the native phase. This is similar to the results from Stern et al. [12] in their phase-resetting analysis. Since we incorporate the analysis of the stable manifolds in this project, we observe how the perturbed orbit can spiral longer inside the basin of attraction of the spiralling equilibria due to the organisational structure imposed by the stable manifolds.

At the end of this project, we repeat the simulations and block the ion regulation across the Ca-dependent BK-channels. In somatotrophs cells, these channels are responsible for burst termination [14]. We superimposed the global attractor on the bifurcation diagram and obtained a global attractor that drops earlier to the lower attracting branch of equilibria even though the global attractor is way too far from the Hopf region. Nevertheless, the global attractor still adheres to the restriction imposed by the stable manifolds, where it drops down as soon as it moves across the basin boundary. Finally, we provide the two-parameter bifurcation diagram for the case of perturbed orbits in the system with blocked BK-channels and deduce that the role played by the stable manifolds is still valid as the limit cycles emanating from a Hopf point move away from the global attractor once we turn on the current. This pronounces the relevance of the stable manifolds mechanism in the termination of burst, as well as method of phase resetting employed by [12], as we prove that one can still reach the same conclusion even without any blocked BK-channels.

## REFERENCES

- [1]Cuthbertson R., Holcombe M., Paton R., *Computation in Cellular and Molecular Biological Systems*, World Scientific Publishing, 1996
- [2]Deininger M., “Cell cycle and growth control: Current clinical applications”, *In: Cell Cycle and Growth Control: Biomolecular Regulation and Cancer*, (Eds) Stein G. S., Pardee A.B., Wiley IEEE, **2**, pp. 669-706, 2004
- [3]Doedel E. J., “AUTO: a program for the automatic bifurcation analysis of autonomous systems”, *Congressus Numerantium*, **30**, pp. 265-284, 1981
- [4]Ermentrout G.B., *Simulating, Analyzing, and Animating Dynamical Systems: A Guide to Xppaut for Researchers and Students*, SIAM Books, 2002
- [5]Hanselman D., Littlefield B., *International edition: Mastering MATLAB 7*, Pearson Education International, 2005
- [6]Hodgkin A., Huxley A., “A quantitative description of membrane current and its application to conduction and excitation in nerve”, *Journal of Neurophysiology*, **117**, pp. 500-544, 1952
- [7]Kaplan D., Glass L., *Understanding Nonlinear Dynamics*, Birkhauser, pp. 37-40, 1995
- [8]Keener J.P., Sneyd J., *Mathematical Physiology*, Springer, 1987
- [9]Kuznetsov Y.A., *Elements of Applied Bifurcation Theory*, Springer, pp. 316–326, 2004
- [10]Raina A.K., Zhu X., Mervyn M., Takeda A., Smith M.A. , “Abortive oncogeny and cell cycle-mediated events in Alzheimer disease”, *In: Progress in Cell Cycle Research*, (Eds) Meijer L., Jézéquel A., Ducommon B., Kluwer Academic/Plenum Publisher, New York, **4**, pp. 235-242, 2000

[11]**Rinzel, J.**, “Bursting oscillations in an excitable membrane model”, *In: Ordinary and Partial Differential Equations, (Eds) Sleeman B.D. & Jarvis R.J.* , Springer-Verlag, New York, **1151**, pp. 68-88, 1985

[12]**Stern J.V., Osinga H.M., LeBeau A., Sherman A.**, “Resetting behavior in a model of bursting in secretory pituitary cells: Distinguishing plateaus from pseudo-plateaus”, *Bulletin of Mathematical Biology*, **70(1)**, pp. 68-88, 2008

[13]**Strogatz, S.H.**, *Nonlinear dynamics and chaos: With applications to physics, biology, chemistry and engineering*, Perseus Publishing, 2001

[14]**Tsaneva-Atanasova K., Sherman A., van Goor F., Stojilkovic S.S.**, “Mechanism of spontaneous and receptor-controlled electrical activity in pituitary”, *Journal of Neurophysiology*, **98**, pp. 131–144, 2007

[15]**Winfree A.T.**, *When Time Breaks Down*, Princeton University Press, Princeton, 1897

## APPENDIX

We provide the auxiliary functions and parameters that describe the right-hand side of equations (1), (2) and (3). The ionic currents flowing through  $Ca$ -channels in equation (3) are expressed as

$$I_C(V) = g_C m_{C_\infty}^2 h_{C_\infty} (V - V_{Ca})$$

where  $C$  stands for  $Ca_T$  or  $Ca_L$ . The constant  $g_C$  is the channel conductance, whereas the steady state function is given by

$$X_\infty(V) = \frac{1}{1 + e^{-\frac{V-V_X}{kX}}}$$

for  $X = m_{Ca_L}, m_{Ca_T}, h_{Ca_T}$ . This function also gives the expression for the steady state function of  $n_{dr}$  in the second ODE of equation (1). The only exception is for the case of  $h_{Ca_L} = 1$ . The ionic currents across  $Na$  and  $K$  are

$$I_{Na}(V) = g_{Ns,Na} (V - V_{Ns,Na}),$$

$$I_K(n_{dr}, V) = I_{K_{dr}} + I_{K_{ir}}.$$

The functions  $K_{dr}$  and  $K_{ir}$  are the delayed-rectifier and inward rectifier currents, respectively. They are expressed as

$$I_Y(n_{dr}, V) = g_Y Y_\infty (V - V_Y)$$

for  $Y = K_{dr}, K_{ir}$  where

$$K_{dr\infty} = n_{dr}; \quad K_{ir\infty}(V) = \frac{\alpha_{ir}}{\alpha_{ir} + \beta_{ir}}.$$

The functions  $\alpha_{ir}$  and  $\beta_{ir}$  are given by

$$\alpha_{ir} = \frac{0.1}{1 + e^{0.06(V - V_{K_{ir}} - 200)}},$$

$$\beta_{ir} = \frac{3e^{2(10^{-4})(V - V_{K_{ir}} - 100)} + e^{10^{-1}(V - V_{K_{ir}} - 10)}}{1 + e^{-0.5(V - V_{K_{ir}})}}.$$

The ionic current across the BK-channels is

$$I_{BK}(Ca, V) = I_{BK_{near}} + I_{BK_{far}},$$

which accounts for two types of BK-channels. Each ionic current is expressed as

$$I_Z = (1 - bkblock) g_Z Z_\infty (V - V_{K_{dr}})$$

for  $Z = BK_{near}, BK_{far}$ . The steady state function is given by

$$Z_{\infty} = \frac{1}{1 + e^{-\frac{V-V_Z}{k_{BK}}}},$$

with the voltage across the BK-channels such that  $V_Z = V_{BK_0} - k_{shift} \ln\left(\frac{Ca_Z}{k_{CaBK}}\right)$ , where

$$Ca_{BK_{near}} = Ca \text{ and } Ca_{BK_{far}}(V) = -A(I_{Ca_L}(V) + I_{Ca_T}(V)).$$

The functions in the ODE for  $Ca$  are

$$\gamma = -f\alpha\beta,$$

$$J(Ca) = -f\beta J_{eff}(Ca) - \mu_{er}Ca + per(Ca_{er} - Ca).$$

The constant  $\beta$  is the ratio between the cell surface area  $A$  to the cell volume (the diameter of the cell is assumed to be  $10.0\mu M$ ),  $\alpha = [2FA]^{-1}$ , where  $F$  is the Faraday constant. The function  $J_{eff}(Ca)$  is given by

$$J_{eff}(Ca) = \frac{\mu_{mp}Ca^2}{Ca^2 + km_{mp}^2}$$

**Table 1** gives all the parameters used in the ODEs and the auxiliary functions.

Parameters	Value	Parameters	Value
$g_{Ca_L}$	0.74 nS	$k_{h_T}$	-5 mV
$g_{Ca_T}$	0.105 nS	$k_{m_L}$	12 mV
$g_{Ns,Na}$	0.1245 nS	$k_{m_T}$	8 mV
$g_{K_{dr}}$	3.85 nS	$k_{n_{dr}}$	8 mV
$g_{K_{ir}}$	15.75 nS	$k_{BK}$	10 mV
$g_{BK_{near}}$	0.55 nS	$k_{Ca_{BK}}$	1.5 mV
$g_{BK_{far}}$	10 nS	$k_{shift}$	18
$V_{Ca}$	60 mV	$km_{mp}$	0.08 $\mu M$
$V_{Ns,Na}$	-20 mV	$A$	0.11
$V_{K_{dr}}$	-80 mV	$\mu_{mp}$	28 $\mu Ms^{-1}$
$V_{K_{ir}}$	-83 mV	$f$	0.009
$V_{BK_0}$	0.1 mV	$c_M$	0.00314 nF
$V_{h_T}$	-56 mV	$\mu_{er}$	0.025 $\mu Ms^{-1}$
$V_{m_L}$	-25 mV	$Ca_{er}$	200
$V_{m_T}$	-45 mV	$p_{er}$	0.00015 $s^{-1}$
$V_{n_{dr}}$	0 mV	$\tau_{n_{dr}}$	0.09 s

**Table 1** Parameter values used in equation (1), (2) and (3).